A Solid-state Refrigeration Design and its Analytical Model

by

Zhimin Sun

Bachelor of Science, Xi'an Jiaotong University, 2010

Master of Engineering, Xi'an Jiaotong University, 2013

Submitted to the Graduate Faculty of

Swanson School of Engineering in partial fulfillment

of the requirements for the degree of

Doctor of Philosophy

University of Pittsburgh

2019

UNIVERSITY OF PITTSBURGH

SWANSON SCHOOL OF ENGINEERING

This dissertation was presented

by

Zhimin Sun

It was defended on

July 1, 2019

and approved by

Dissertation Director: William Slaughter, Ph.D., Associate Professor,
Department of Mechanical Engineering and Materials Science

Qing-Ming Wang, Ph.D., Professor,
Department of Mechanical Engineering and Materials Science

Patrick Smolinski, Ph.D., Associate Professor,
Department of Mechanical Engineering and Materials Science

Guangyong Li, Ph.D., Associate Professor,
Department of Electrical and Computer Engineering

A Solid-state Refrigeration Design and its Analytical Model

Zhimin Sun, Ph.D.

University of Pittsburgh, 2019

Conventional cooling technology is a very mature technology and had been widely used in industry. However, it has many disadvantages, like environmental pollution and large space to store the device, etc. In order to solve the disadvantages and satisfy current industry requirements, many novel cooling technologies have been explored. Among them, electrocaloric cooling technology attracts a lot of attention due to its outstanding properties, where it has reversible temperature change of a polarizable material with the application of an electric field. Thus, many cooling device designs based on electrocaloric effect have been developed. However, there are two main drawbacks caused by designs to control heat transfer process. One is heat transfer fluid medium loss and the other is moving part requirements (either moving electrocaloric materials or moving fluid medium). The purpose of this thesis is for developing a new and smart heat transfer controlling method. The core design is a composite where electrocaloric layer and substrate layer are bonded together. The composite has temperature change due to electrocaloric effect with application of electric field. In the meantime, it also has converse piezoelectric effect, and thus can bend upward or downward to connect with heat source (or heat sink) for transferring heat. An analytical model is also studied and proposed by considering multi-physical effects in the composite structure, which provides a new way to explore the mechanism of solid-state cooling technology accurately. Our analytical model shows that the temperature change is a combined result from thermal, electric and mechanical field couplings, not just one coupling from electrocaloric effect, which is widely known as Indirect Method derived from Maxwell Equations.

Moreover, the model clearly demonstrates that material properties, boundary conditions of the composite, electric field influence cooling performance. The rest of the thesis thoroughly studies various electrocaloric materials, substrate materials, boundary conditions, cooling composite shape. The results show a very promising way to improve cooling performance.

Table of Contents

List of Tables

List of Figures

Preface

The basis for the research originally stemmed from my passion for developing better method to control heat transfer process in electrocaloric based solid-state cooling technology, which has great potential to solve urgent cooling issues and corresponding environment problems. As the world moves further into the digital age, highly efficient microelectronic cooling devices are urgently required. Studying and researching at the University of Pittsburgh provides me an opportunity to do the cutting-edge research.

In truth, I would like to express my sincere appreciation to my advisors, Professor William Slaughter and Professor Qing-Ming Wang for their support and guidance through my graduate studies. My committee members, Professor Guangyong Li and Professor Patrick Smolinski have provided valuable advices and suggestions about my research. I am also thankful for my colleagues and friends whom I was pleasure to work with: Dr. Yangzhan Yang, Ms. Qiuyan Li and Mr. Pei-Yuan Hsiao, and Dr. Hongfei Zu. At last, I would like to thank my parents Jiangzhong Sun and Ronghua Yuan, and my husband Yangxi Ou for their unconditional love and support. Thank you all for your unwavering support!

1.0 Introduction

This chapter reviews different cooling technologies, and their advantages and disadvantages. Among them, electrocaloric (EC) cooling technology, which has reversible temperature change of a polarizable material in an adiabatic condition with the application and/or removal of an electric field, exhibits some great potentials for efficient solid-state refrigeration. The history of EC cooling technology and device design is reviewed for better understanding. At the last section of the chapter we propose our research focus and the significance of this thesis research.

1.1 Motivations

Conventional vapor compression technique has dominated the cooling device market for over one hundred years. It is no doubt that the technique is very mature, applicable, and current device design can maximize the cooling efficiency. However, the most efficient refrigerants to drive these cooling systems are Freon gases or chlorofluorocarbons and hydrochlorofluorocarbons, which are harmful to ozone and result in increase of ultraviolet (UV) radiation exposure. The rise in UV radiation exposure has led to increasing possibility of skin cancers and other public health problems [1]. Therefore, many researchers are working to find new refrigeration techniques and eliminate these bad environmental consequences.

Finding new cooling technologies is also an urgent requirement for industry. For example, in recent years electronic miniaturization has drawn great attention due to growing demand for

lightweight and small devices in microelectronics industry. In these electronic miniaturizations a chip may be comprised of thousands of components, which results in large heat generation due to Joule heat [2]. The performance of the electronics highly depends on the cooling efficiency. However, conventional cooling technology can not satisfy the small device volume requirement. Therefore, future development of the industry relies closely on the development of solid-state cooling technologies.

Currently, there are some solid-state cooling technologies which have received great attention due to their advantages and potential substitution for the conventional vapor cooling. But they also have disadvantages to limit their applications. Table 1.1 lists some widely developed solid-state cooling technologies with their efficiency and evaluation.

Table 1. 1. Efficiency in different cooling technologies [3-5]

Novel cooling technology	**Efficiency (%)**	**Evaluations**
Thermoelectric cooler	10	Compactness, expensive and low efficiency
Electrocaloric cooler	60-70	Compactness, cost reduction
Magnetocaloric cooler	60-70	Large magnetic field is required
Conventional vapor cooler	40-50	Very mature, less progress in the market

Thermoelectric cooling is a solid-state cooling technology converting electric energy into a temperature gradient known as Peltier effect [5], which creates a heat flux at the junction of two different types of materials. The primary advantages are its lack of moving parts or circulating liquid and thus it has very long life time. The device can be in small size and flexible shape.

However, it has main drawbacks due to the expensive thermoelectric materials and its intrinsic low efficiency (maximum 10%), the application is highly limited. Many researchers and companies are looking for cost reduced alternative materials and ways to improve efficiency.

Magnetocaloric cooler is based on magnetocaloric effect. When a magnetic field is applied onto a ferromagnetic material, the magnetic domains are orientated along the direction of the applied magnetic field, which lowers entropy due to the spin arrangement from less order state to order state, and consequently raises material temperature. Some researchers argue that the first discovery of magnetocaloric effect is controversy: some believe that Warburg found it in 1881, while others think it should be credited to P. Weiss and A. Piccard in 1917 [6]. This cooling technology has been employed for achieving ultralow temperatures in research laboratories for decades and led to the Nobel Prize in chemistry being awarded to Giauque in 1949. Magnetocaloric refrigerator is also a good candidate which is more energy efficient than the conventional vapor cooling devices. However, current magnetocaloric refrigerators are formed by large and expensive superconducting materials or heavy permanent magnets for the purpose of inducing large magnetic fields, which limits the viability of magnetic cooling in the market [7].

Electrocaloric cooler is analogous to the magnetocaloric cooler, while the only difference is that temperature change is induced by electrocaloric effect instead of magnetocaloric effect. The electrocaloric effect is the dipolar entropy and consequently temperature change when an electric field is applied to a polar material under adiabatic conditions. Studies show that refrigeration based on the EC effect has greater potential advantages over magnetocaloric coolers: higher power densities, compactness, smaller mass of a device, potential cost reduction, no dependence on rare-earth materials, etc. Thus, solid-stare coolers based on electrocaloric effect have attracted a lot of attentions from both academy and industry [8].

1.2 Electrocaloric Effect

1.2.1 Development of Electrocaloric Effect

Electrocaloric phenomenon was first proposed theoretically as the converse effect of pyroelectricity by William Thomson in 1878 [9] and the experimental observation was first found in Rochelle salt by Hautzenlaub in 1943 [10], in which the electrocaloric temperature change was only ~0.003 K. Twenty years later Karchevskii found that the maximum temperature change was discovered to exist around Curie Temperature in most of material systems, which demonstrated the potential relation between electrocaloric effect and ferroelectric phase transition [11]. Among this period, on one hand, research on electrocaloric materials was directed by specific industry demands. Superconductivity was popular which worked below 15K. Consequently, electrocaloric materials with low phase transition temperature were developed and tested by Raghebaugh in $SrTiO_3$ and $KTaO_3$ systems in 1977 with temperature change of 0.3K [12]. On the other hand, room temperature operation also stimulated exploring electrocaloric materials with phase transition around room temperature. $Pb(Zr_{0.455}Sn_{0.455}Ti_{0.09})O_3$ was studied with temperature change of 1.6K for room temperature cooling applications [13].

However, in the following decades after the first discovery of electrocaloric effect, few efforts were put into the development of electrocaloric cooling technology. The main reason was that electrocaloric temperature change was very small compared with conventional vapor cooling method and magnetocaloric cooling technology, which weakened industry interest in electrocaloric cooling technology. But the attitude toward electrocaloric cooling technology changed significantly in 2006 since a giant electrocaloric effect discovery was found in $PbZr_{0.95}Ti_{0.05}O_3$ thin film with a large temperature change of 12K [14]. The phenomenon was

attributed to the fact that the breaking-down electric field is larger in thin films than bulks. Another giant electrocaloric effect was discovered in polyvinylidene fluoride-trifluoroethylene [P(VDF-TrFE)] thin films with temperature change of 12K two years later [8]. Figure 1.1 shows publication quantity versus year of publication, which clearly demonstrates that giant electrocaloric effect discovery in year of 2016 is a turning point, after which electrocaloric research has drawn more attention.

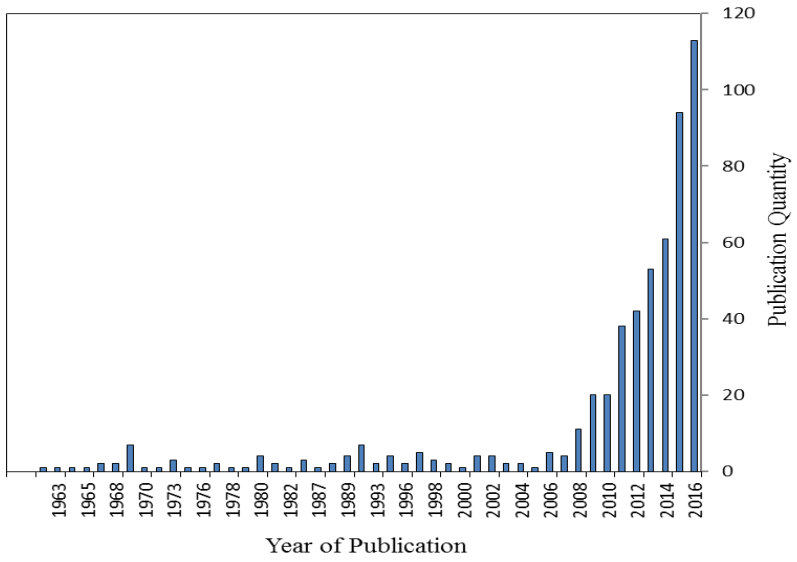

Figure 1. 1. Statistics of publication quantity vs. year of publication from Web of Science data.

Recent investigations have also put forward a "negative electrocaloric effect", in which the sign of change of temperature is reversed. The positive and negative electrocaloric effects were found in relaxor $70PbMg_{1/3}Nb_{2/3}O_3$-$30PbTiO_3$ single crystals across the phase diagram [15]. The discovery of the negative electrocaloric effect sheds light on the understanding of electrocaloric mechanism.

1.2.2 Electrocaloric Cooling Principle

Ferroelectric materials have a unique property that the polarization direction can be reoriented by the application of an external electric field and thus materials show macroscopic polarization, shown in Figure 1.2.

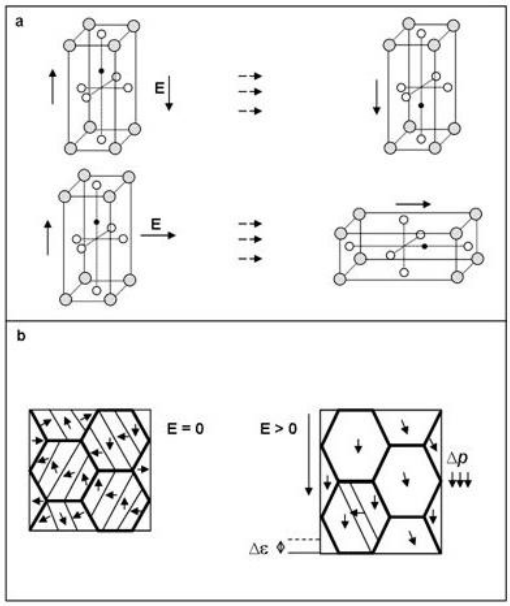

Figure 1. 2. The application of an electric field causes (a) the reorientation of a spontaneous polarization in a unit cell to the field direction; (b) the sum of the microscopic piezoelectricity of the polarization of the domains results in the macroscopic polarization of the ferroelectrics.

Figure 1.2(a) illustrates the polarization direction is changed by the direction of the external electric field. Polar-disordered ferroelectric domains with macroscopic zero polarization turn to polar-ordered state with macroscopic residual polarization by the domains elongating in the downward direction with external electric field, illustrated in Figure 1.2(b).

The electrocaloric effect is manifested in the heating or cooling of a ferroelectric material due to the applied electric field under adiabatic conditions shown in left part of Figure 1.3. The application of the electric field causes change of the dipolar state in an electrocaloric material, from less ordered state to more ordered state, which results in entropy decreasing. As a result, the temperature of the material increases due to the lattice vibration entropy compensation of the reduction of the dipolar entropy adiabatically. At this time, the electrocaloric material releases heat to heat sink through heat transfer process and then the temperature of the material turns to the original state. When the electric field is removed from the electrocaloric material, dipoles turn back to less ordered state again followed by entropy increasing. Therefore, the temperature of the material decreases due to the lattice vibration entropy reduction of the increment of the dipolar entropy adiabatically. In the meantime, the electrocaloric material absorbs heat from heat source and at last temperature increases again. The process is repeatable and steady-state occurs after enough circles. Such electrocaloric heating or cooling cycle is comparable to a corresponding heating or cooling cycle taking place in a classic compression vapor cycle illustrated in the right part of Figure 1.3. The gas temperature change is achieved by changing the gas pressure, while in contrast the EC material temperature change is achieved by a change of the electric field.

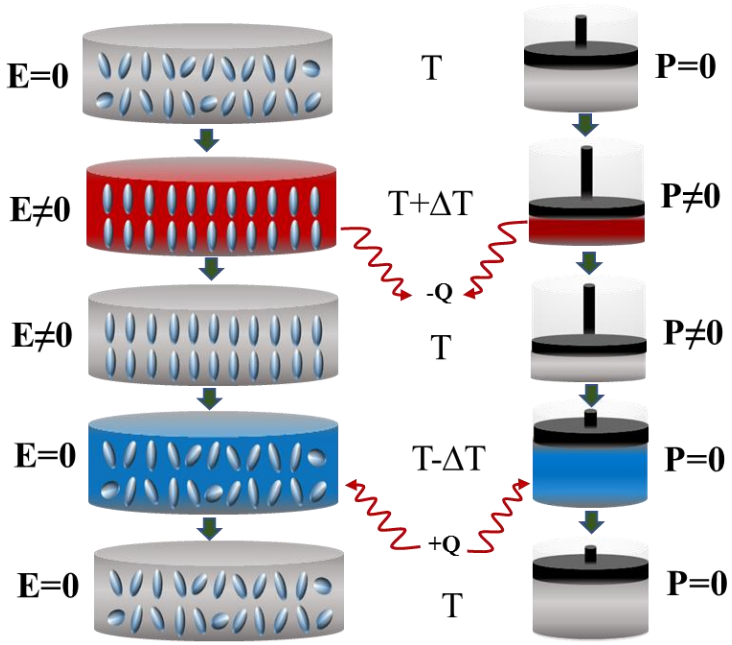

Figure 1. 3. Schematic vapor cycle representation of the electrocaloric cycle and the classic compression. The working coolant is a ferroelectric material in the EC cycle and a vapor in the classic compression vapor cycle.

1.2.3 Theory of Electrocaloric Effect

It is well established that the EC effect is a thermodynamic phenomenon, which can be understood in terms of standard thermodynamic relations [16]. The Gibbs free energy density G of a dielectric material is expressed as a function of temperature T, entropy S, stress X, strain x, electric field E, and dielectric polarization P.

In differential form, it can be written as

$$dG = -SdT - x_i X_i - P_i dE_i \tag{1.1}$$

from which it follows that

$$S = -\left(\frac{\partial G}{\partial T}\right)_{X,P}, x_i = -\left(\frac{\partial G}{\partial X_i}\right)_{T,P}, P_i = -\left(\frac{\partial G}{\partial E_i}\right)_{T,X} \quad (1.2)$$

The variable pairs (S, T) and (P, E) satisfy the standard Maxwell relation

$$(\frac{\partial S}{\partial E_i})_{T,X} = (\frac{\partial P_i}{\partial T})_{E,X} \quad (1.3)$$

Assuming a constant stress X, the entropy change during an adiabatic process is given by

$$dS = (\frac{\partial S}{\partial E})_T dE + (\frac{\partial S}{\partial T})_E dT = 0 \quad (1.4)$$

From the definition of heat capacity per unit volume

$$C_E = \rho c_E = T(\frac{\partial S}{\partial T})_E \quad (1.5)$$

Therefore, by inserting the definition of heat capacity per unit volume expressed in Eq. (1.5) into Eq. (1.4), the temperature, pressure and electric field are related with the density and the heat capacity of electrocaloric material.

$$(\frac{dT}{dE})_S = -\frac{T}{\rho c_E}(\frac{\partial P}{\partial T})_E \tag{1.6}$$

By formally integrating equation, one obtains the adiabatic temperature change

$$\Delta \mathrm{T} = -\int_{E_1}^{E_2} \frac{T}{\rho c_E}(\frac{\partial P}{\partial T})_E dE \tag{1.7}$$

which describes the value of the temperature change during an adiabatic variation of the field E.

In practical application of equation, the usual input data consist of the experimental values for the dielectric polarization P(E, T) and the heat capacity c(E, T). By evaluating the integral numerically, a value for the EC temperature change is obtained. This procedure is known as the indirect method of determining the EC effect.

Since it is nontrivial to solve the integral equation, several simplifying steps are needed. First, the discrete experimental points for P(E, T) can be fitted with a polynomial, thus allowing the derivative with respect to T and subsequent integration over E to be performed. Second, the temperature and field dependence of the heat capacity is often neglected and a representative value of c is moved in front of the integral. Then equation predicts a smooth variation of ΔT with temperature and electric field.

Thus, the isothermal entropy change ΔS is given by

$$\Delta \mathrm{S} = \int_{E_1}^{E_2} (\frac{\partial P}{\partial T})_E dE \tag{1.8}$$

1.3 Electrocaloric Device Concepts

Electrocaloric devices can be mainly classified into five categories according to different conditions in Figure 1.4. Translational fluidic active electrocaloric regenerator (AER) is a device type that fluid medium is inside of the device which requires either movement of EC material or heat transfer medium for transferring heat between heat sink and heat source. If both movements of EC material and heat transfer medium occur in the device, it is rotating fluidic AER, a special device type in translational fluidic AER. When fluid medium does not exist in the devices and either movement of EC material or heat transfer medium is required for transferring heat, it is translational solid AER. One special device type in the translational solid AER is rotating solid AER. The last device type is thermal diode EC cooler, which does not require fluid medium and movement of EC material and heat transfer medium [17].

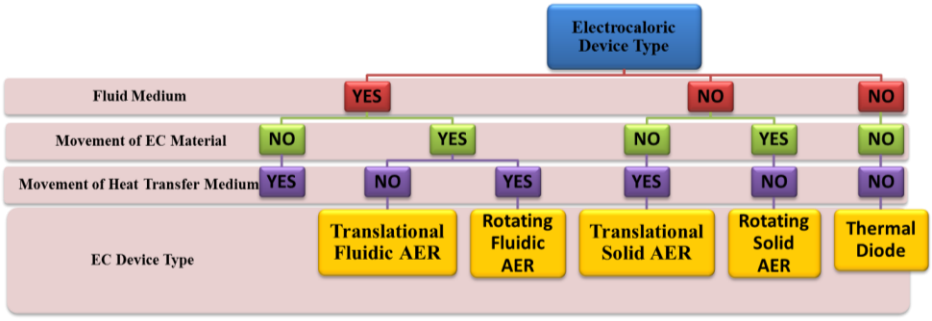

Figure 1. 4. Classification of EC cooling devices.

1.3.1 Translational fluidic AER

A prominent device type is translational fluidic AER, which has fluid medium inside the device. A schematic setup is illustrated in Figure 1.5. It mainly consists of a fluidic bed with an active regenerator (EC material) in its center, a heat exchanger on each side and a driving mechanism like a pump used for alternately pushing the fluid back and forth through the regenerator.

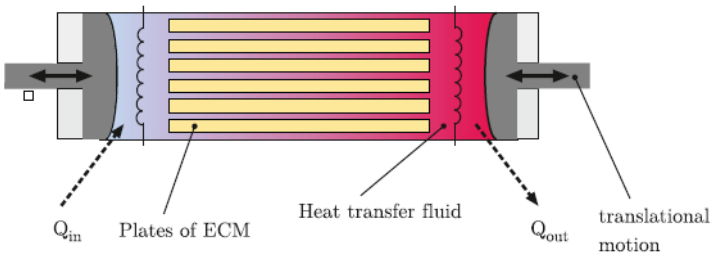

Figure 1. 5. Schematic setup of a translational fluidic AER and translational solid ARE. Reprinted from [17], with the permission of EPL Publishing.

To achieve a cooling on one of the heat exchangers, the cooling cycle depicted in Figure 1.6 is carried out: In the initial state, all components of the system are at the same temperature and the fluid is pushed to one side. During the first step, the EC material is polarized by applying an electric field. Thus, the temperature of the EC material increases by ΔT. While the electric field is on, the fluid is pushed to the opposite direction, absorbing heat from the EC material and delivering it to the hot heat exchanger. In the third step, the field is turned off which results in the decrease of the EC material temperature. The fluid is pushed back through the EC material, releasing heat

to the EC material and reaching the cold heat exchanger at a lower temperature. The fluid can then absorb heat and the cycle is repeated from the first step. After several cycles, a temperature gradient is established along the device. The translational fluidic AER is the device type which has been studied most than any other EC cooling devices.

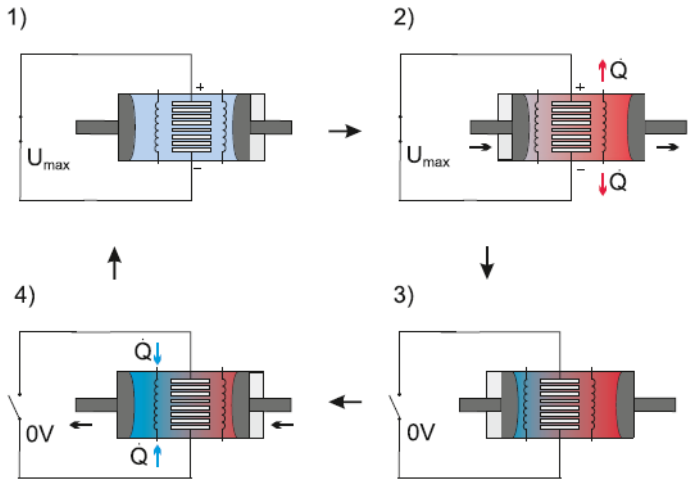

Figure 1. 6. Schematic function principle for a translational fluid AER. Reprinted from [17], with the permission of EPL Publishing.

The first demonstrator of an AER was developed by Sinyavsky and Brodyansky with a temperature span of 5K in a 55 mm long device [18]. The possibly most advanced design of a complete cooling device can be found in Guo et al. [19] showing a temperature span of 15K. The advantages of the translational fluidic AER are a relatively easy setup, good heat transfer between fluid and solid. While the main disadvantages are losses associated with fluid flow. Therefore, the significant challenges are long-term stability and reliability. In summary, the type is the most mature EC cooling device.

1.3.2 Rotating Fluid AER

A device with fluidic heat transfer medium and moving EC material can be realized with a rotating wheel on which the EC material is located. In this rotating fluidic AER, a continuously flowing heat transfer fluid is conducted from a heat source through or along a part of the wheel, and then to the heat sink and back along the opposite part of the wheel to heat source, shown in Figure 1.7. The top part of EC rings is activated with application of electric field and the EC temperature increases before it gets in contact with the fluid flowing from the heat source. The heat is released from the top part of EC rings to fluid medium and then fluid medium flows to heat sink to reject heat. When the top part of EC rings rotates outside of high field region and locates at the bottom, the temperature of this part decreases and when it connects with fluid medium from heat sink, it absorbs heat from the fluid medium which results in temperature decrease of fluid medium. In the last step, fluid medium flows back to the heat source and absorbs heat from the heat source.

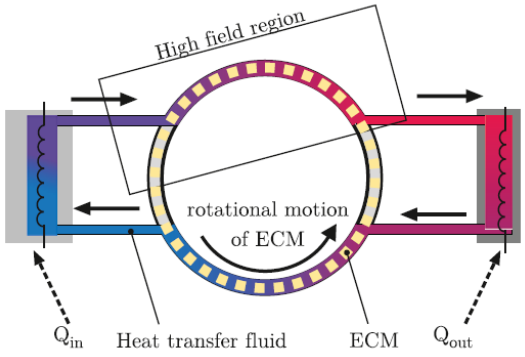

Figure 1. 7. Schematic working principle of rotating fluidic AER. Reprinted from [17], with the permission of EPL publishing.

This concept is well-known from magnetocaloric cooling [20]. However, it is not favorable in electrocaloric cooling. Challenges are numerous, especially sealing and electrical connection. In the meantime, this device type requires two moving systems and may have large fluid flow losses.

1.3.3 Translational Solid AER

The translational solid AER is basically working in the same cooling principles as the translational fluidic AER with the fluid being replaced by solid-state plates. The working principles consist of four steps shown in Figure 1.8 [21]: (a) the EC material moves to the right side of regenerator, and the electric field increases from 0 to E_o; (b) the EC material is fixed on the right side for a time period, heat is ejected from EC material to the regenerator; (c) the EC material moves to the left side of regenerator, and the electric field decreases from E_o to 0; (d) the EC material stays at the left side for a time period and absorbs heat from the regenerator at the cold end. As the refrigeration cycle repeats, heat will be transported by the EC material from the left side to the right side, and a temperature gradient is established within both the EC material and regenerator.

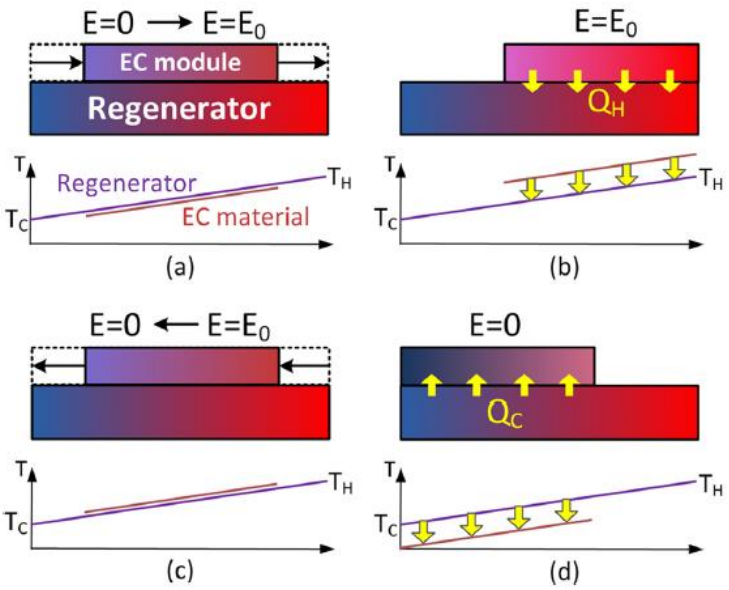

Figure 1. 8. An illustration of the operation principle of translational solid AER. Reprinted from [21], with the permission of AIP Publishing.

The concept of a translational solid-state AER has been described by Li et al. [22]and a first conceptual cooling device design with a corresponding demonstrator has been presented in 2013 by Gu et al. [21, 23]. In their work, the translational solid AER consists of two 24-layer EC modules and four stainless steel regenerators, illustrated in Figure 1.9. Thermal insulators were placed at the very top and bottom of the device to prevent heat dissipation along the z direction. The EC modulus was fixed to a frame, and the regenerators were driven by a step motor to generate a cyclic motion with respect to the EC modulus. A remarkable temperature span of 6.6K could be achieved after the steady-state is reached.

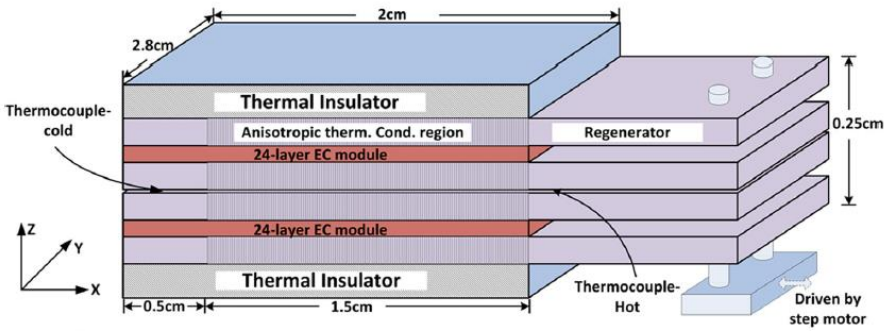

Figure 1. 9. Schematic of the translational solid AER. Reprinted from [21], with the permission of AIP Publishing.

The translational solid AER is advantageous compared with translational fluid AER in the following aspects. First, solid state device can be easily and accurately driven and controlled by miniature actuators, and consequently the whole device can reduce to chip scale. Second, solid state device has no mixing problem that happens in liquid. While it has many advantages, it has issues of performance which is highly influenced by the heat transfer between the plates, friction, wear and external system like step motor.

1.3.4 Rotating Solid AER

Rotating solid AER is also similar to the rotating fluidic AER with moving EC material but with solid heat transfer medium. This concept was proposed in 2014 by Gu et al. [24]. Figure 1.10 illustrates schematically the proposed EC refrigerator, which consists of stacked EC rings, and each EC ring is composed of 16 EC elements, separated by small gaps of low thermal conductivity. The EC rings rotate coaxially with the same rotating speed but rotating in opposite directions. Each neighboring EC rings are in direct contact to facilitate heat exchange. Heat

exchangers with high thermal conductivity are placed outside of these two neighboring EC rings at the cold and hot ends to absorb or reject heat. The two directly contacted EC rings, along with the heat exchangers, can be treated as a single unit of the refrigerator. Heat transfer between the heat exchangers which are located on two opposing sides of the discs is realized by synchronized rotation and polarizing of the EC elements. The elements alternatively deliver and take heat from the adjacent discs. A detailed description of the function principle is provided in Ref. [24].

The theoretical temperature change is 20K while it must be noted that losses due to friction are not accounted for. The advantages, disadvantages and challenges are similar to the ones of the translational fluidic AER. Additionally, tighter geometrical restrictions apply and the countercurrent rotation of adjacent discs may be difficult to practically realize.

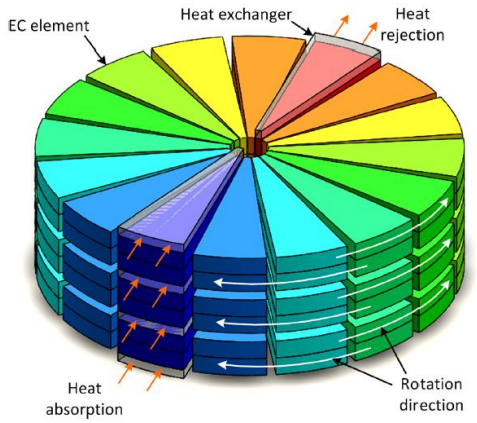

Figure 1. 10. Schematic setup of a rotating fluidic AER. Reprinted from [24], with the permission of AIP Publishing.

1.3.5 Thermal diode EC device

Device type without moving EC material or heat transfer medium can be built as a thermal diode EC device. Instead of moving the EC elements, additional elements to control the heat flow direction are integrated between the EC elements, seen in Figure 1.11. The thermal diodes can turn "on" or "off" to control heat transfer direction [25]. In Figure 1.11, it clearly shows that heat is transferred from multilayer (electrocaloric materials) to heat sink in the left figure, while heat is dumped to multilayer from heat source in the right figure.

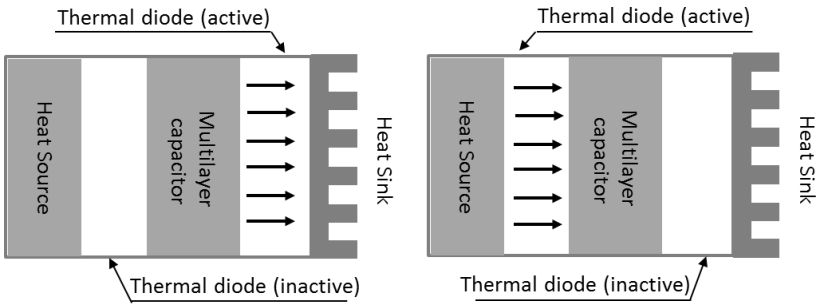

Figure 1. 11. Thermal diodes to control heat transfer direction. In left figure, the left thermal diode is off while the right one is on, resulting heat transferring from multilayer capacitor to heat sink; in the right figure, heat transfers from heat source to multilayer capacitor as the left thermal diode is on while the right one is off.

A thermal diode would consist of liquid crystals, in which thermal conductance is strongly anisotropic, shown in Figure 1.12 [26]. When the liquid crystal's director is mainly parallel to the plane, the thermal conductivity across the film is k_{low}. When the director is mainly perpendicular to the film, the thermal conductivity across the film is enhanced to k_{high}. The orientation of the

liquid crystal's directors can be controlled by electric fields applied across the liquid crystal. One possibility is that the surface of the material confining the liquid crystal can be textured so that the director is parallel to the plane when there is no applied electric field and perpendicular when a voltage is applied.

Clearly, the performance of such devices is strongly limited by the performance of the thermal diodes. The desired ideal behavior of the thermal diodes is to perfectly conduct heat in "on" state and insulate in "off" state. Thus, achieving a high conductivity ratio in the thermal diodes is the most important challenge in device design.

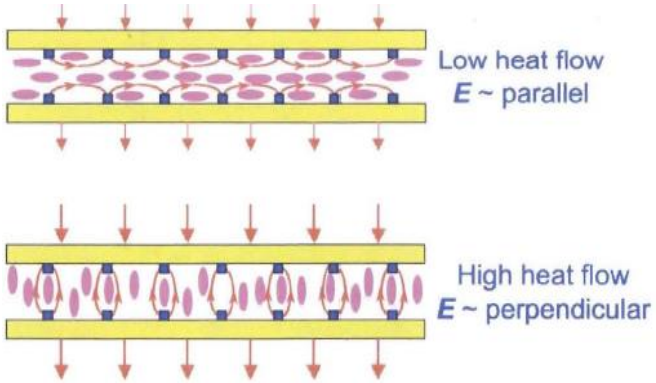

Figure 1. 12. Edge view of a liquid crystal heat diode. The liquid crystal's directors can be switched between predominately parallel to the film of liquid crystal (top panel) to mainly perpendicular to the film (bottom panel). Reprinted from [26], with the permission of AIP Publishing.

1.3.6 Summary

The advantages and disadvantages of different EC device types are summarized in Table 1-2. The main challenges for the current device designs are the fluid flow loss, friction, finite conductivity ratio, etc.

Table 1. 2. Advantages and disadvantages of EC cooling device types

Device Type	Translational fluidic AER	Rotating fluidic AER	Translational solid AER	Rotating solid AER	Thermal diodes
Advantages	Good thermal contact; easy design	Suitable for externally applied fields	No passive heat transfer medium; no fluid loss	No passive heat transfer media; no fluid loss	No moving part; no fluid; compact device
Disadvantages	Fluid flow loss; moving part	Two moving systems; large fluid flow losses	Friction, wear	Friction, wear; geometrical restriction	Limited switching frequency; finite conductivity ratio

1.4 Research Purpose

Electrocaloric (EC) cooling technology has a promising future due to its advantages over conventional cooling methods and many efforts have been input into EC device designs. In the device designs, one of the main challenges is how to separate EC material from heat source and heat sink, and thus to control the heat transfer direction. Previous device types require movement of EC material by step motor or fluid media by pump back and forth between heat source and heat sink for controlling heat transfer process. On the other hand, other device design utilizes thermal

diodes by adjusting their thermal conductivity to control heat transfer direction. These are all efficient ways to control heat transfer direction. However, many drawbacks occur like fluid medium loss and moving part requirement. Here in our thesis we want to design a new and smart way to control heat transfer process. The hypnosis comes from the combination of converse piezoelectric effect and electrocaloric effect. The core design utilizes bending performance when there is deformation difference between two bonded layers and thus controls heat transfer process. Another research focus is how to analyze the working performance of the design. Our analytical model considers multi-physical effects in the core design and shows that the temperature change is a combined result from thermal, electrical and mechanical field couplings, which provides a thorough way to understand the electrocaloric cooling mechanism.

We believe our thesis of "A solid-state refrigeration device design and its analytical model" will draw great interest from the physical, mechanical, thermal and technology communities. Because of the above-mentioned novelties and physical insight, we believe that this work will be interesting for both designers and theorists.

2.0 Design and Analytical Model of The Novel Solid-state EC Refrigeration

A design concept of smart method to control heat transfer process is presented in this chapter. The core design has two same composites, each of which is comprised by an EC layer and a substrate layer bonded together. The temperature of the composite is changed with application of the electric field due to electrocaloric effect. The composite also has converse piezoelectric effect, and thus can bend upward or downward by the application of electric field. In addition, an analytical model is studied which indicates the temperature change is a combined result from thermal, electrical and mechanical field couplings. Moreover, the model shows that material properties, boundary conditions, electric field define the cooling performance.

2.1 Design Concept

The core component can be described as a set of two same composites, each of which is EC layer (top) and substrate layer (bottom) bonded together illustrated in Figure 2.1 [27]. The EC layers are coated with silver electrodes for electric field application. These two composites are implemented in a system that comprises a heat sink, a heat source, an electric field generator and an insulated shell. Inside the device, it is in vacuum atmosphere for the prevention of heat convection.

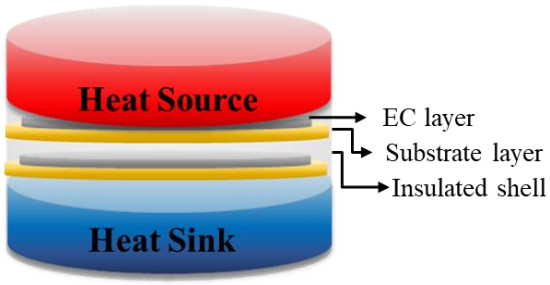

Figure 2. 1. Configuration of the novel EC device.

A schematic presentation of such a system and its cycling working steps are presented in Figure 2.2. The design combines converse piezoelectric effect and electrocaloric effect. The converse piezoelectric effect enables device to control heat transfer process, which means transferring heat in one direction from heat source to the cooling composite and finally to heat sink. The electrocaloric effect enables temperature of the cooling composite decreasing when the cooling composite connects with heat source, while increasing when it connects with heat sink. Therefore, the device design can eliminate the drawbacks existed in previous electrocaloric devices.

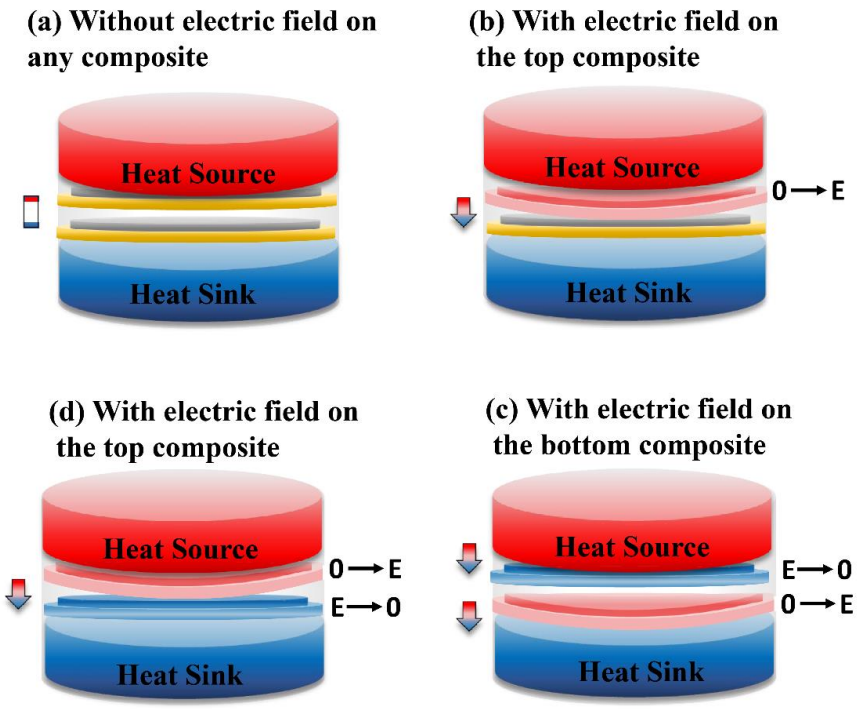

Figure 2. 2. A schematic diagram of the solid-state refrigerator and its cycling working steps. The arrow points out to the heat transfer direction. (a) The composites are in their equilibrium positions without the application of electric field. The top surface of the EC layer in the top composite is closely connected with the heat source and the bottom composite is not connected with any part of the device. (b) When the electric field is applied across the thickness of the EC layer in the top composite, it bends downward to connect with the bottom composite with its temperature increasing and heat is transferred. (c) When the electric field is removed from the top composite and applied to the bottom one, the top composite turns to the equilibrium position with connecting with the heat source and heat is transferred from heat source to it due to its temperature decreasing. In the meantime, the bottom composite bends to connect with heat sink and transfers heat to heat sink due to its temperature increasing. (d) Electric field is applied to the top composite and removed from the bottom one. The top composite bends downward and the bottom one goes back to its original position, where they are connected. Heat is transferred from the top composite to the bottom one due to electrocaloric effect. Reprinted from [27], with the permission of AIP Publishing.

At the beginning without the application of electric field, the two composites are in their original positions: the top surface of the EC layer in the top composite is closely connected with heat source and the bottom composite is not connected with the top composite or heat sink, shown in Figure 2.2(a). When the electric field is applied across the thickness of the EC layer in the top composite, the EC layer contracts due to the converse piezoelectric effect while the substrate layer resists the deflection, which leads the composite to bend downward and connect with the bottom composite. The temperature of the top composite increases in the adiabatic condition resulted from intensity of polarization increasing due to the electrocaloric effect and thus heat is transferred from the top composite to the bottom one, illustrated in Figure 2.2(b). With the removal of the electric field from the top composite and the application of electric field to the bottom one, the opposite electric field modes make the two composites show different behaviors, illustrated in Figure 2.2(c). The polar dipoles in the EC layer of the top composite turn to disorder again, which results in the temperature decreasing in the adiabatic condition. In the meantime, the composite turns to its original position and connects with heat source again. Therefore, heat is transferred from the heat source to the top composite. Meanwhile, the bottom composite bends downward to connect with heat sink due to the converse piezoelectric effect and its temperature increases in the adiabatic condition due to the electrocaloric effect. Heat is released from the bottom composite to the heat sink. In Figure 2.2(d), the electric field is applied to the top composite while removed from the bottom one, which makes the composite behaviors shown in Figure 2.2(c) turned-over. Heat is transferred from the top composite to the bottom one. After several cycles of process (c) and (d), temperature of the heat source decreases. In the scenario illustrated above, it clearly shows that novel solid-state refrigeration is achieved without movement of either EC material or fluid media by external assistance.

2.2 Analytical Model of The Novel Refrigeration

2.2.1 Analytical model

The analytical model is based on Kirchoff's Theory (also known as classical plate theory CPT) [28], which works well when the ratio of radius to thickness of plates is more than ten times. Some assumptions are made in the model: (1) The layers are bonded to each other perfectly in no-slip boundary condition; (2) The material of each layer is linearly elastic and transversely isotropic; (3) Each layer has uniform thickness and properties in each layer are homogeneous; (4) The contact thermal resistances between layers are neglected and thus heat transfer is fast enough to get homogeneous temperature distribution within the composite. In addition, the piezoelectric material is assumed to be a polycrystalline ceramic poled along the axis (z axis) normal to the surface, and therefore the in-plane strains due to the poling field are isotropic and the in-plane piezoelectric coefficients are isotropic, i.e., $d_{31}=d_{32}$; (5) The model does not consider dielectric loss and mechanical loss.

The composite constitutes by an EC layer and a substrate layer bonded together. With application of electric field, EC layer made of piezoelectric material has deformation due to the converse piezoelectric effect while substrate layer made of copper or steel resists the deformation. Therefore, strain and stress are induced in the composite under clamped-edge boundary condition. A cylindrical (r-ɵ-z) coordinate is located at the mid-plane of the bottommost layer (reference plane) and the z-axis is taken upward from the reference plane. The k_{th} layer is located between the points $z=z_{k-1}$ and $z=z_k$ in the thickness direction (k=1, substrate layer; k=2, EC layer). From Kirchoff's theory, the strain and the curvature for the plate at the reference plane can be expressed in terms of the lateral and transverse deflections of points in that plane as:

$$\begin{Bmatrix} \varepsilon_{rr}^{0} \\ \varepsilon_{\theta\theta}^{0} \end{Bmatrix} = \begin{Bmatrix} \dfrac{\partial u_0(r)}{\partial r} \\ \dfrac{u_0}{r} \end{Bmatrix} \text{ and } \begin{Bmatrix} k_r^0 \\ k_\theta^0 \end{Bmatrix} = \begin{Bmatrix} -\dfrac{\partial^2 w_0(r)}{\partial r^2} \\ -\dfrac{1}{r}\dfrac{\partial w_0(r)}{\partial r} \end{Bmatrix} \tag{2.1}$$

where $u_0(r)$ is the lateral deflection and $w_0(r)$ is the transverse deflections of points in the reference plane, ε_{rr}^0 and $\varepsilon_{\theta\theta}^0$ are the radial and the tangential strains at the reference plane, and k_r^0 and k_θ^0 are the radial and tangential curvatures of the reference plane, respectively. The in-plane shear component $\varepsilon_{r\theta}^0$ is omitted as only axisymmetric deformation is considered. By assuming a linear distribution of strain along the thickness direction, the transversely isotropic strain in k_{th} layer of the structure at a distance z from the reference plane is described in terms of the strain and curvature of the reference plane as [29]:

$$\begin{Bmatrix} \varepsilon_{rr}^{k} \\ \varepsilon_{\theta\theta}^{k} \end{Bmatrix} = \begin{Bmatrix} \varepsilon_{rr}^{0} \\ \varepsilon_{\theta\theta}^{0} \end{Bmatrix} + z \begin{Bmatrix} k_r^0 \\ k_\theta^0 \end{Bmatrix} - E_f^k \begin{Bmatrix} d_{31}^k \\ d_{31}^k \end{Bmatrix} \tag{2.2}$$

where E_f^k is the applied external electric field across the k_{th} layer and d_{31}^k is the transverse piezoelectric constant for the k_{th} layer. If the k_{th} layer is a piezoelectric material layer, d_{31}^k is nonzero. However, if the k_{th} layer is non-piezoelectric material layer, then it is zero.

The linear isotropic strain-stress relation for the k_{th} layer in the polar coordinate system is:

$$\begin{Bmatrix} \sigma_{rr}^{k} \\ \sigma_{\theta\theta}^{k} \end{Bmatrix} = [Q_k] \begin{Bmatrix} \varepsilon_{rr}^{k} \\ \varepsilon_{\theta\theta}^{k} \end{Bmatrix} = [Q_k] \left(\begin{Bmatrix} \varepsilon_{rr}^{0} \\ \varepsilon_{\theta\theta}^{0} \end{Bmatrix} + z \begin{Bmatrix} k_r^0 \\ k_\theta^0 \end{Bmatrix} - E_f^k \begin{Bmatrix} d_{31}^k \\ d_{31}^k \end{Bmatrix} \right) \tag{2.3}$$

where σ_{rr}^{k} and $\sigma_{\theta\theta}^{k}$ are the stresses in radial and tangential directions of the k_{th} layer, and $[Q_k]$ is the plane stress-reduced stiffness matrix of the k_{th} layer expressed in terms of engineering constants as:

$$[Q_k] = \frac{E_k}{1 - v_k^2}\begin{bmatrix} 1 & v_k \\ v_k & 1 \end{bmatrix} \tag{2.4}$$

The net force N, and the net moment M, acting on the structure across the entire plate thickness is obtained by integrating the stresses through the thickness of each layer of the plate and then summing the forces and moments over all the layers as:

$$\mathbf{N} = \begin{Bmatrix} N_r \\ N_\theta \end{Bmatrix} = \sum_{\boldsymbol{k=1}}^{\boldsymbol{n}} \int_{\boldsymbol{z_{k-1}}}^{\boldsymbol{z_k}} \begin{Bmatrix} \sigma_{rr}^{k} \\ \sigma_{\theta\theta}^{k} \end{Bmatrix} dz = \boldsymbol{A}\begin{Bmatrix} \varepsilon_{rr}^{0} \\ \varepsilon_{\theta\theta}^{0} \end{Bmatrix} + \boldsymbol{B}\begin{Bmatrix} k_r^{0} \\ k_\theta^{0} \end{Bmatrix} - \begin{Bmatrix} N_r^{p} \\ N_\theta^{p} \end{Bmatrix} \tag{2.5a}$$

$$\mathbf{M} = \begin{Bmatrix} M_r \\ M_\theta \end{Bmatrix} = \sum_{\boldsymbol{k=1}}^{\boldsymbol{n}} \int_{\boldsymbol{z_{k-1}}}^{\boldsymbol{z_k}} \begin{Bmatrix} \sigma_{rr}^{k} \\ \sigma_{\theta\theta}^{k} \end{Bmatrix} z dz = \boldsymbol{B}\begin{Bmatrix} \varepsilon_{rr}^{0} \\ \varepsilon_{\theta\theta}^{0} \end{Bmatrix} + \boldsymbol{D}\begin{Bmatrix} k_r^{0} \\ k_\theta^{0} \end{Bmatrix} - \begin{Bmatrix} M_r^{p} \\ M_\theta^{p} \end{Bmatrix} \tag{2.5b}$$

where N_r and N_θ are the components of the net force in the radial and tangential directions and M_r and M_θ are the components of the net moment in the radial and tangential directions, **A**, **B** and **D** are the extensional stiffness matrix, extensional-bending coupling stiffness matrix, and bending stiffness matrix, respectively, expressed as:

$$\mathbf{A} = \begin{bmatrix} A_{11} & A_{12} \\ A_{12} & A_{11} \end{bmatrix} = \sum_{k=1}^{n} \int_{z_{k-1}}^{z_k} [Q_k] dz$$

$$= \begin{bmatrix} \sum_{k=1}^{n} \frac{E_k}{1-v_k^2}(z_k - z_{k-1}) & \sum_{k=1}^{n} \frac{v_k E_k}{1-v_k^2}(z_k - z_{k-1}) \\ \sum_{k=1}^{n} \frac{v_k E_k}{1-v_k^2}(z_k - z_{k-1}) & \sum_{k=1}^{n} \frac{E_k}{1-v_k^2}(z_k - z_{k-1}) \end{bmatrix} \tag{2.6a}$$

$$\mathbf{B} = \begin{bmatrix} B_{11} & B_{12} \\ B_{12} & B_{11} \end{bmatrix} = \sum_{k=1}^{n} \int_{z_{k-1}}^{z_k} [Q_k] z dz$$

$$= \begin{bmatrix} \sum_{k=1}^{n} \frac{E_k}{2(1-v_k^2)}(z_k^2 - z_{k-1}^2) & \sum_{k=1}^{n} \frac{v_k E_k}{2(1-v_k^2)}(z_k^2 - z_{k-1}^2) \\ \sum_{k=1}^{n} \frac{v_k E_k}{2(1-v_k^2)}(z_k^2 - z_{k-1}^2) & \sum_{k=1}^{n} \frac{E_k}{2(1-v_k^2)}(z_k^2 - z_{k-1}^2) \end{bmatrix} \tag{2.6b}$$

$$\mathbf{D} = \begin{bmatrix} D_{11} & D_{12} \\ D_{12} & D_{11} \end{bmatrix} = \sum_{k=1}^{n} \int_{z_{k-1}}^{z_k} [Q_k] z^2 dz$$

$$= \begin{bmatrix} \sum_{k=1}^{n} \frac{E_k}{3(1-v_k^2)}(z_k^3 - z_{k-1}^3) & \sum_{k=1}^{n} \frac{v_k E_k}{3(1-v_k^2)}(z_k^3 - z_{k-1}^3) \\ \sum_{k=1}^{n} \frac{v_k E_k}{3(1-v_k^2)}(z_k^3 - z_{k-1}^3) & \sum_{k=1}^{n} \frac{E_k}{3(1-v_k^2)}(z_k^3 - z_{k-1}^3) \end{bmatrix} \tag{2.6c}$$

N_r^p and N_θ^p are the radial and tangential equivalent piezoelectric forces, and M_r^p and M_θ^p are the radial and tangential equivalent piezoelectric moments generated by the piezoelectric material layer under voltage load when the structure is fully constrained and expressed as:

$$\boldsymbol{N^p} = \begin{Bmatrix} N_r^p \\ N_\theta^p \end{Bmatrix} = \sum_{k=1}^{n} \int_{z_{k-1}}^{z_k} [Q_k] E_f^k \begin{Bmatrix} d_{31}^k \\ d_{31}^k \end{Bmatrix} dz = \begin{Bmatrix} \sum_{k=1}^{n} \frac{E_k d_{31}^k E_f^k (z_k - z_{k-1})}{1 - v_k} \\ \sum_{k=1}^{n} \frac{E_k d_{31}^k E_f^k (z_k - z_{k-1})}{1 - v_k} \end{Bmatrix} \tag{2.7a}$$

$$\boldsymbol{M^p} = \begin{Bmatrix} M_r^p \\ M_\theta^p \end{Bmatrix} = \sum_{k=1}^{n} \int_{z_{k-1}}^{z_k} [Q_k]\, z E_f^k \begin{Bmatrix} d_{31}^k \\ d_{31}^k \end{Bmatrix} dz = \begin{Bmatrix} \sum_{k=1}^{n} \dfrac{E_k d_{31}^k E_f^k (z_k^2 - z_{k-1}^2)}{2(1 - v_{k)}} \\ \sum_{k=1}^{n} \dfrac{E_k d_{31}^k E_f^k (z_k^2 - z_{k-1}^2)}{2(1 - v_k)} \end{Bmatrix} \tag{2.7b}$$

The net force and moment on the structure, N and M hold the structure in static equilibrium, which axis-symmetrically loaded conditions can be expressed as [30]:

$$\frac{dN_r}{dr} + \frac{N_r - N_\theta}{r} = 0 \tag{2.8a}$$

$$\frac{dQ_z}{dr} + \frac{Q_z}{r} = 0 \tag{2.8b}$$

where Q_z is the vertical shear force that varies in the radial direction. The shear force Q_z can be expressed in terms of the net moments in the radial direction as:

$$Q_z = \frac{dM_r}{dr} + \frac{M_r - M_\theta}{r} \tag{2.9}$$

Putting the equations of force and moment (2.7a) and (2.7b) into the governing equations of (2.8a) and (2.8b), the following differential equations about transverse and lateral deflections are obtained:

$$A_{11}\left(\frac{\partial^2 u_0(r)}{\partial r^2}+\frac{1}{r}\frac{\partial u_o(r)}{\partial r}-\frac{u_0(r)}{r^2}\right)+B_{11}\left(-\frac{\partial^3 w_0(r)}{\partial r^3}-\frac{1}{r}\frac{\partial^2 w_o(r)}{\partial r^2}+\frac{1}{r^2}\frac{\partial w_0(r)}{\partial r}\right)=0 \quad (2.10a)$$

$$B_{11}\left(\frac{\partial^2 u_0(r)}{\partial r^2}+\frac{1}{r}\frac{\partial u_o(r)}{\partial r}-\frac{u_0(r)}{r^2}\right)+D_{11}\left(-\frac{\partial^3 w_0(r)}{\partial r^3}-\frac{1}{r}\frac{\partial^2 w_o(r)}{\partial r^2}+\frac{1}{r^2}\frac{\partial w_0(r)}{\partial r}\right)=Q_z \quad (2.10b)$$

Then combining equations by eliminating $u_0(r)$, a differential equation entirely in terms of the transverse deflection $w_0(r)$ is obtained:

$$\left(-\frac{\partial^3 w_0(r)}{\partial r^3}-\frac{1}{r}\frac{\partial^2 w_o(r)}{\partial r^2}+\frac{1}{r^2}\frac{\partial w_0(r)}{\partial r}\right)\frac{A_{11}B_{11}-B_{11}^2}{A_{11}}=Q_z \quad (2.11)$$

Next by substituting the expression (2.9) for Q_z and rearranging terms, a differential equation relating the transverse deflection $w_0(r)$ is obtained:

$$\left(\frac{\partial^4 w_0(r)}{\partial r^4}+\frac{2}{r}\frac{\partial^3 w_o(r)}{\partial r^3}-\frac{1}{r^2}\frac{\partial^2 w_o(r)}{\partial r^2}+\frac{1}{r^3}\frac{\partial w_0(r)}{\partial r}\right)=0 \quad (2.12)$$

The general solution for transverse deflection $w_0(r)$ is obtained as:

$$w_0(r)=c_1r^2+c_2lnr+c_3r^2lnr+c_4 \quad (2.13)$$

where c_1, c_2, c_3 and c_4 are the constants of integration.

Next, a governing differential equation for the lateral deflection $u_0(r)$ is obtained:

$$\left[\frac{\partial^2 u_0(r)}{\partial r^2} + \frac{1}{r}\frac{\partial u_o(r)}{\partial r} - \frac{u_0(r)}{r^2}\right] - \frac{4}{r}\frac{B_{11}}{A_{11}}c_3 = 0 \tag{2.14}$$

The general solution for lateral deflection $u_0(r)$ is obtained as:

$$u_0(r) = c_3\frac{B_{11}}{A_{11}}r(2lnr - 1) + c_5 r + \frac{c_6}{r} \tag{2.15}$$

where c_5 and c_6 are the additional constants of integration.

2.2.2 Boundary Conditions

When the diameter of piezoelectric layer is not equal to the substrate layer, it is partially covered situation. The analytical solutions for deflections are obtained by applying the above derived relations to two sections: exterior annulus plate ($R_i<r<R_0$) and interior core laminate ($0<r<R_i$), separately and then connecting them through matching continuity and equilibrium conditions at the interface of the two sections [31]. Expressions for transverse and lateral deflections of the exterior annulus and the interior core sections, respectively, are obtained as follows:

$$w_{ext}(r) = c_1 r^2 + c_2 lnr + c_3 r^2 lnr + c_4 \quad (2.16a)$$

$$u_{ext}(r) = \frac{1}{16}\frac{B_{11}^{ext}}{(A_{11}^{ext}D_{11}^{ext} - B_{11}^{ext\,2})} r^3 P + c_3 \frac{B_{11}^{ext}}{A_{11}^{ext}} r(2lnr - 1) + c_5 r + \frac{c_6}{r} \quad (2.16b)$$

$$w_{int}(r) = \frac{1}{64}\frac{A_{11}^{int}}{(A_{11}^{int}D_{11}^{int} - B_{11}^{int\,2})} r^4 P + c_7 r^2 + c_8 lnr + c_9 r^2 lnr + c_{10} \quad (2.16c)$$

$$u_{int}(r) = \frac{1}{16}\frac{B_{11}^{int}}{(A_{11}^{int}D_{11}^{int} - B_{11}^{int\,2})} r^3 P + c_9 \frac{B_{11}^{int}}{A_{11}^{int}} r(2lnr - 1) + c_{11} r + \frac{c_{12}}{r} \quad (2.16d)$$

where A_{11}^{ext}, B_{11}^{ext}, D_{11}^{ext} and A_{11}^{int}, B_{11}^{int} , D_{11}^{int} are the stiffness coefficients for the exterior annulus and the interior core sections, respectively. Constants c_1-c_{12} are 12 constants to be evaluated next by applying appropriate boundary conditions at the interface of the interior core and the exterior annulus sections. However, equations are simplified by setting constants c_8=c_9=c_{12}=0 so that $w_{int}(r)$ and $u_{int}(r)$ are numerically defined at r=0 and the equations remain valid in the entire range of their applicability: 0<r<R_i. The fixed boundary conditions on the outer plate r=R_o on the outer annular region viz. $w_{ext}(R_0) = 0$, $\frac{\partial w_{ext}(R_0)}{\partial r} = 0$, $u_{ext}(R_0) = 0$ yield the following respective equations:

$$c_1 R_0^2 + c_2 lnR_0 + c_3 R_0^2 lnR_0 + c_4 = 0 \quad (2.17a)$$

$$2c_1R_0 + c_2\frac{1}{R_0} + c_3R_0(1 + 2lnR_0) = 0 \tag{2.17b}$$

$$c_3\frac{B_{11}^{ext}}{A_{11}^{ext}}(2lnR_0 - 1)R_0 + c_5R_0 + c_6\frac{1}{R_0} = 0 \tag{2.17c}$$

The continuity and equilibrium conditions at r=R_i, the interface of the exterior annulus and the interior core sections, viz. $w_{int}(R_i) = w_{ext}(R_i)$, $\frac{\partial w_{ext}(R_0)}{\partial r} = \frac{\partial w_{int}(R_0)}{\partial r}$, $u_{int}(R_i) = u_{ext}(R_i)$, $N_{r,ext}(R_i) = N_{r,int}(R_i)$, $M_{r,ext}(R_i) = M_{r,int}(R_i)$, $Q_{r,ext}(R_i) = Q_{r,int}(R_i)$, yield the following respective equations:

$$c_1R_i^2 + c_2lnR_i + c_3\ln(R_i)\,R_i^2 + c_4 - c_7R_i^2 - c_{10} = 0 \tag{2.17d}$$

$$2c_1R_i + c_2\frac{1}{R_i} + c_3R_i(1 + 2lnR_i) - 2c_7R_i = 0 \tag{2.17e}$$

$$c_3\frac{B_{11}^{ext}}{A_{11}^{ext}}(2lnR_i - 1)R_i + c_5R_i + c_6\frac{1}{R_i} - c_{11}R_i - c_{11}R_i = 0 \tag{2.17f}$$

$$\begin{aligned} &2(B_{11}^{ext} + B_{12}^{ext})c_1 - \frac{(B_{11}^{ext} - B_{12}^{ext})}{R_i^2}c_2 - (A_{11}^{ext} + A_{12}^{ext})c_5 \\ &+ \frac{(A_{11}^{ext} - A_{12}^{ext})}{R_i^2}c_6 - 2(B_{11}^{ext} + B_{12}^{ext})c_7 + (A_{11}^{ext} + A_{12}^{ext})c_{11} = N_r^p \end{aligned} \tag{2.17g}$$

$$-2(D_{11}^{ext}+D_{12}^{ext})c_1+\frac{D_{11}^{ext}-D_{12}^{ext}}{R_i^2}c_2+(B_{11}^{ext}+B_{12}^{ext})c_5$$
$$-\frac{(B_{11}^{ext}-B_{12}^{ext})}{R_i^2}c_6+2(D_{11}^{ext}+D_{12}^{ext})c_7-(B_{11}^{ext}+B_{12}^{ext})c_{11}=-M_r^p \quad (2.17h)$$

$$-\frac{4}{R_i}\frac{A_{11}^{ext}D_{11}^{ext}-{B_{11}^{ext}}^2}{A_{11}^{ext}}c_3=0 \quad (2.17i)$$

Finally, constants c_1-c_{12} can be solved by the above matrix equation through Matlab (Details in Appendix A). Therefore, the expression of $w_{ext}(r)$, $u_{ext}(r)$, $w_{int}(r)$ and $u_{int}(r)$ are defined. For the interior part, the strain and stress can be solved by inserting equation (2.16(c)-(d)) into equations (2.1) -(2.2).

$$\begin{Bmatrix}\varepsilon_{rr,int}^k\\ \varepsilon_{\theta\theta,int}^k\end{Bmatrix}=\begin{Bmatrix}c_{11}-2c_7z-E_f^k d_{31}^k\\ c_{11}-2c_7z-E_f^k d_{31}^k\end{Bmatrix} \quad (2.18a)$$

$$\begin{Bmatrix}\sigma_{rr,int}^k\\ \sigma_{\theta\theta,int}^k\end{Bmatrix}=\frac{E_k}{(1-v_k)}\begin{Bmatrix}c_{11}-2c_7z-E_f^k d_{31}^k\\ c_{11}-2c_7z-E_f^k d_{31}^k\end{Bmatrix} \quad (2.18b)$$

The entropy change is:

$$dS_{int}^k=\alpha^k d\left(\sigma_{rr,int}^k+\sigma_{\theta\theta,int}^k\right)-p^k dE_f^k+\frac{c^k\rho_k}{T}dT \quad (2.19)$$

where p^k, ρ^k, α^k and c^k are the pyroelectric coefficient, density, thermal conductivity and specific heat capacity of the k_{th} layer respectively. The first term in equation (2.19) is caused by piezocaloric effect, the second term is from electrocaloric effect in EC layer and the third term is due to lattice vibration.

For the external annulus part, the strain and stress can be solved by inserting equations (2.16(a)-(b)) into equations (2.1) -(2.2):

$$\begin{Bmatrix} \varepsilon_{rr,ext}^k \\ \varepsilon_{\theta\theta,ext}^k \end{Bmatrix} = \begin{Bmatrix} c_5 - \frac{c_6}{r^2} + z(\frac{c_2}{r^2} - 2c_1) \\ c_5 + \frac{c_6}{r^2} - z(\frac{c_2}{r^2} + 2c_1) \end{Bmatrix} \tag{2.20a}$$

$$\begin{Bmatrix} \sigma_{rr,ext}^k \\ \sigma_{\theta\theta,ext}^k \end{Bmatrix} = \frac{E_k}{1-v_k^2} \begin{Bmatrix} (1+v_k)c_5 + (v_k-1)\frac{c_6}{r^2} + z(\frac{c_2}{r^2} - 2c_1 - 2c_1 v_k - \frac{c_2 v_k}{r^2}) \\ (1+v_k)c_5 + (1-v_k)\frac{c_6}{r^2} + z\left(\frac{c_2 v_k}{r^2} - 2c_1 - 2c_1 v_k - \frac{c_2}{r^2}\right) \end{Bmatrix} \tag{2.20b}$$

The entropy change is defined as:

$$dS_{ext}^k = \alpha^k d\left(\sigma_{rr,ext}^k + \sigma_{\theta\theta,ext}^k\right) + \frac{c^k \rho_k}{T} dT \tag{2.21}$$

Therefore, the entropy changes of each layer in the composite, as an extensive property, is derived by integrating the entropy change in equation (2.19) and equation (2.21) through the volume of each layer.

$$dS_{int}^{pz} = \pi R_i^2 \alpha^{pz} \frac{E_{pz} t_{pz}}{1 - v_{pz}} \left[c_{11}' dE_f - c_7' \left(t_{pz} + t_s \right) dE_f - d_{31} dE_f \right] - \frac{\pi R_i^2 t_{pz}}{2} p dE_f + \frac{\pi R_i^2 c^{pz} t_{pz} \rho_{pz}}{2T} dT \tag{2.22a}$$

$$dS_{int}^{s} = \frac{\pi R_i^2 \alpha^s E_s t_s}{1 - v_s} c_{11}' dE_f + \frac{\pi R_i^2 c^s t_s \rho_s}{2T} dT \tag{2.22b}$$

$$dS_{ext}^{s} = \frac{\pi (R_o^2 - R_i^2) \alpha^s E_s t_s}{1 - v_s} c_5' dE_f + \frac{\pi (R_o^2 - R_i^2) c^s \rho_s t_s}{2T} dT \tag{2.22c}$$

Where $c_i' = c_i / E_f$(i=1,2,3…12). Therefore, the total entropy change rate is obtained as:

$$\mathrm{dS} = dS_{int}^{pz} + dS_{int}^{s} + dS_{ext}^{s} \tag{2.23}$$

In an adiabatic process, the total entropy change is zero so that the temperature change of the composite is derived as:

$$\left(\frac{\pi R_i^2 c^{pz} t_{pz} \rho_{pz} + \pi R_o^2 c^s t_s \rho_s}{2T} \right) dT + \left(\frac{A - \pi R_i^2 t_{pz} p}{2} \right) dE_f = 0 \tag{2.24}$$

where A=2($\frac{\pi R_i^2 \alpha^{pz} E_{pz} t_{pz}}{1-v_{pz}} c_{11}' - \frac{\pi R_i^2 \alpha^{pz} E_{pz} t_{pz}}{1-v_{pz}} \left(t_{pz} + t_s\right) c_7' - \frac{\pi R_i^2 \alpha^{pz} E_{pz} t_{pz}}{1-v_{pz}} d_{31} + \frac{\pi R_i^2 \alpha^s E_s t_s}{1-v_s} c_{11}' +$ $\frac{\pi (R_o^2 - R_i^2) \alpha^s E_s t_s}{1-v_s} c_5'$). Since the pyroelectric coefficient p is not a constant but varies with electrical field $-(\frac{\partial P}{\partial T})_E$, the temperature change is:

$$\Delta T = -\int_0^{E_f} \frac{T\left(A + \pi R_i^2 t_{pz} (\frac{\partial P}{\partial T})_E\right)}{\pi R_i^2 t_{pz} c^{pz} \rho_{pz} + \pi R_o^2 t_s c^s \rho_s} dE_f \tag{2.25}$$

By inducing volume ratio $w_{pz} = \frac{\pi R_i^2 t_{pz}}{\pi R_i^2 t_{pz} + \pi R_o^2 t_s}$ and $w_s = \frac{\pi R_o^2 t_s}{\pi R_i^2 t_{pz} + \pi R_o^2 t_s}$, equation (2.25) can be rewritten as:

$$\Delta T = -\int_0^{E} \frac{T\left(A' + \omega_{pz} (\frac{\partial P}{\partial T})_E\right)}{\overline{\rho c}} dE \tag{2.26}$$

where $\overline{\rho c} = \omega_{pz} c^{pz} \rho_{pz} + \omega_s c^s \rho_s$, is the average density timing heat capacity of the composite, $A' = 2(\frac{\omega_{pz} \alpha^{pz} E_{pz}}{1-v_{pz}} c_{11}' - \frac{\omega_{pz} \alpha^{pz} E_{pz}}{1-v_{pz}} \left(t_{pz} + t_s\right) c_7' - \frac{\omega_{pz} \alpha^{pz} E_{pz}}{1-v_{pz}} d_{31} + \frac{\omega_s \alpha^s E_s t_s}{1-v_s} c_5' + \frac{\omega_{pz} \alpha^s E_s t_s}{(1-v_s) t_{pz}} (c_{11}' -$ c_5') is defined as a correct factor.

The corresponding entropy change is expressed as：

$$\Delta \mathrm{S} = -\int_0^E \frac{\bar{c}\left(A' + \omega_{pz}(\frac{\partial P}{\partial T})_E\right)}{\overline{\rho c}}\, dE \tag{2.27}$$

where $\bar{c}$ is the average specific heat capacity of the composite as $\bar{c} = \omega_{pz}c^{pz} + \omega_s c^s$.

2.2.3 Model Evaluation

Equation (2.17) is in a similar format when compared with the indirect method which is derived from Maxwell relation $\Delta \mathrm{T} = -\int_0^E \frac{T(\frac{\partial P}{\partial T})_E}{\rho_{pz} C_{pz}} dE$, whereas some differences exist: (1) Indirect method is derived by only considering EC material in the adiabatic process, while the present work considers both the EC layer and the substrate layer; (2) The analytical model is based on multi-physical effects of the mechanical field, electrical field and thermal field couplings, while indirect method only considers electrocaloric effect in respect of piezoelectric material. It is clearly that if the composite reduces to one EC layer which is in free boundary condition, equation (2.17) is the same as the indirect method derived from Maxwell relation.

2.3 Results and Discussion

2.3.1 Electrocaloric and Substrate Materials

EC material is $BaTiO_3$ ferroelectric which is a strong EC lead-free alternative due to a large latent heat and a sharp phase transition [32]. $BaTiO_3$ is a ferroelectric oxide that undergoes a transition from a ferroelectric tetragonal phase to a paraelectric cubic phase upon heating above 130^{o}C. In cubic perovskite $BaTiO_3$, titanium atoms are octahedrally coordinated by six oxygen atoms shown in Figure 2.3 (a). Ferroelectricity in tetragonal $BaTiO_3$ is due to an average relative displacement along the z-axis of titanium from its centrosymmetric position in the unit cell and consequently the creation of a permanent electric dipole. The tetragonal unit cell is shown in Figure 2.3(b). The elongation of the unit cell along the z-axis is used as an indication of the presence of the ferroelectric phase.

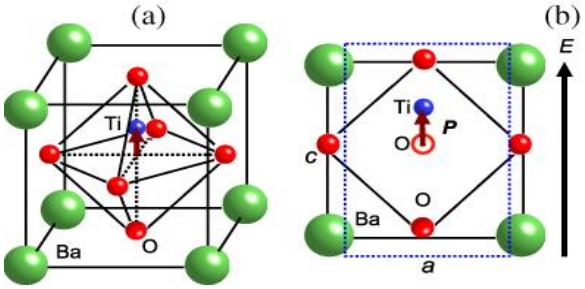

Figure 2. 3. Unit cell of $BaTiO_3$ in (a) cubic cell and (b) a tetragonal cell [32].

For the substrate layer, copper is used since it is one of best substrate materials for high thermal conductivity and ductility. The physical properties of $BaTiO_3$ and Cu are listed in Table 2.1.

Table 2. 1. Physical properties of $BaTiO_3$ and Cu

	Density (kg/m^3)	Heat capacity ($J/(kg \cdot K)$)	Thermal expansion coefficient (K^{-1})	Piezoelectric Coefficient (m/V)	Young's modulus (N/m^2)	Poison's ratio
$BaTiO_3$	6020	434	6.17×10^{-6}	2×10^{-11}	6.7×10^{10}	0.23
Cu	8920	390	17.7×10^{-6}	-----	11×10^{10}	0.34

2.3.2 Electrocaloric Results

Polarization as a function of electric field in $BaTiO_3$ at temperature range from 323K to 423K is shown in Figure 2.4 [32]. At lower temperature 323K, the hysteresis loop indicates $BaTiO_3$ is in ferroelectric phase, while the slim shape at higher temperature 423K illustrates the paraelectric phase in $BaTiO_3$.

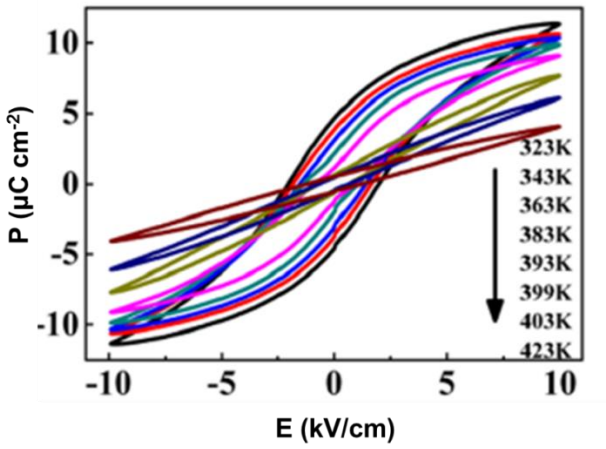

Figure 2. 4. Typical ferroelectric hysteresis loop in $BaTiO_3$.

If the up-part of the ferroelectric hysteresis loop is considered, polarization values at each temperature are taken for different set of electrical fields, shown in Figure 2.5. It is clearly illustrated that ferroelectric transition in $BaTiO_3$ is not a strong first-order ferroelectric transition.

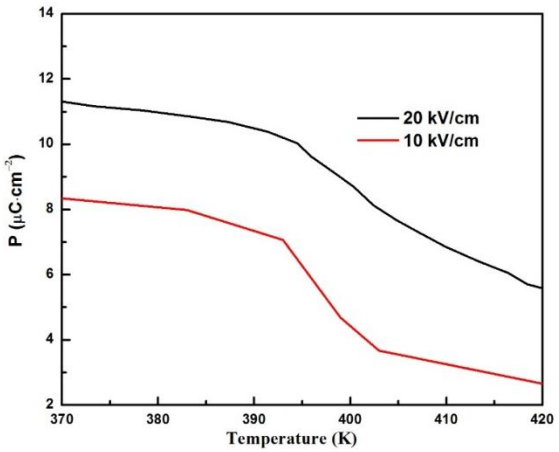

Figure 2. 5. Polarization as a function of temperature under 20kV/cm and 10kV/cm respectively.

The polarization with respect to temperature is illustrated in Figure 2.6 as a function of temperature under electric field of 20kV/cm, 1 kV/cm and 5kV/cm, respectively. The value is lowest around the phase transition temperature and there is not obvious difference among these three curves.

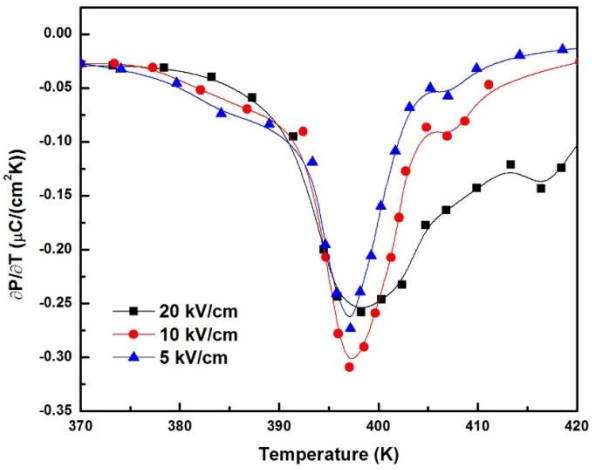

Figure 2. 6. Polarization with respect to temperature under electric field of 20kV/cm, 10kV/cm and 5kV/cm.

Figure 2.7 illustrates the temperature change and the corresponding entropy change under electric field of 5kV/cm, 10kV/cm and 20kV/cm respectively when the thickness of substrate layer and EC layer is 0.1mm and 0.3mm, and the radius is 1.27mm and 0.889mm, respectively. The maximum temperature change occurs around the phase transition temperature, which has good agreement with previous publications. When the electric field is 20kV/cm, the maximum of temperature change is 0.42K while the maximum of temperature change is 0.24K under 10kV/cm and 0.11K under 5kV/cm, which indicates the temperature change is lager under higher electric

field. Peak under 20kV/cm shifts rightward, demonstrating that electric field favors the low symmetry phase and thus the phase transition temperature increases. Figure 2.7(b) is the corresponding entropy change of the composite. The maximum value of entropy change is obtained also around the phase transition temperature, which are 0.43J/(K·kg), 0.25J/(K·kg) and 0.11J/(K·kg) under 20kV/cm, 10kV/cm and 5kV/cm, respectively. When the work temperature is away from the T_c, the entropy changes decrease dramatically. Therefore, the results show that refrigerator performs best around phase transition temperature and when the working temperature is far away from phase transition temperature, the electrocaloric effect is highly suppressed and cooling efficiency is very low.

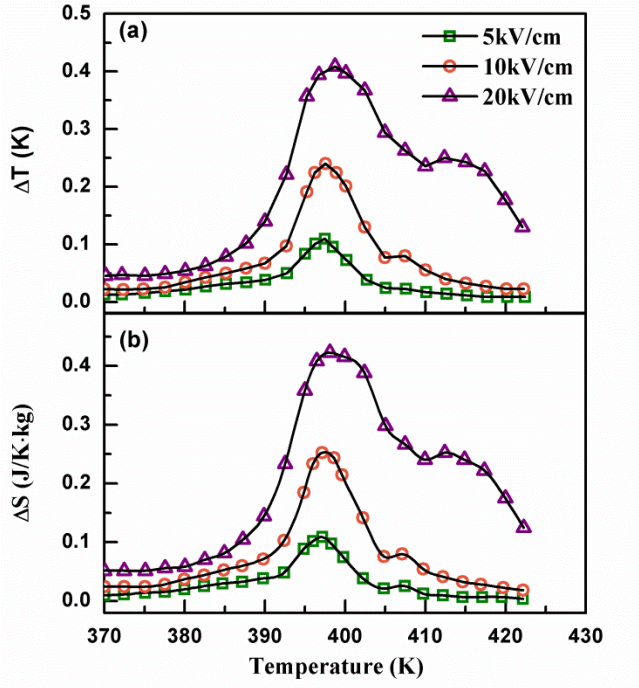

Figure 2. 7. (a) Temperature change and (b) entropy change of composite.

Figure 2.8 shows the 3-D diagram about the relation between temperature change, entropy change and thickness ratio and radius ratio. It clearly shows with increase ratio of thickness and radius, the temperature and entropy changes both increase.

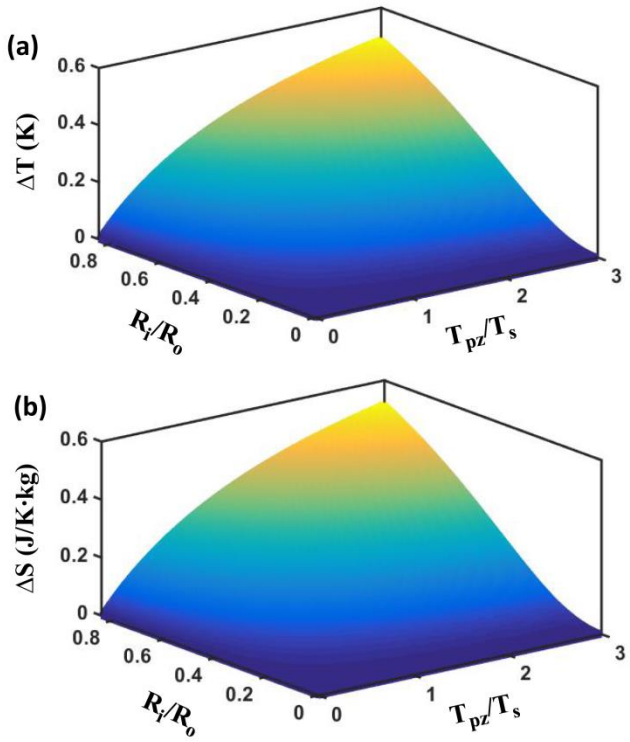

Figure 2. 8. (a) Temperature change and (b) the corresponding entropy change as a function of the ratio of thickness and the ratio of radius of EC layer to substrate layer at 397K under 20kV/cm.

According to the conservation of energy, the input energy is electrical energy and the output energy is in three formats: electrical energy, mechanical energy and thermal energy. When the EC layer takes the largest volume ratio ($\omega_{pz} = 1$) which means no substrate layer, the electrocaloric effect is favored most and the temperature change would be the largest under free

boundary condition which value is 0.79K at 397K under 20kV/cm. It is noted that since part of the input energy is converted into mechanical energy due to the converse piezoelectric effect, the temperature change derived from equation (2.17) is smaller than the theoretical temperature change from indirect method. However, additional energy is not required to move EC material or fluid media in this novel solid-state refrigerator and thus the energy conversion rate may be still the same as previous reported device designs.

Working principle of the present composite requires bending performance and therefore volume ratio of EC layer cannot be very large. In the meantime, volume ratio of EC layer cannot be very small due to cooling requirement. By the calculation derived from equation (2.17), the largest center deflection appears when the ratio of radius R_i/R_o is 0.7. If the ratio of thickness T_{pz}/T_s is 3, the center deflection is half of the center deflection as the thicknesses of EC layer and substrate layer are equivalent, while the temperature change of the composite is twice of the temperature change when T_{pz}/T_s is designed to be 1. Thus, the optimal design of the solid-state refrigerator is when the radius ratio (R_i/R_o) is set to be 0.7 and the thickness ratio (T_{pz}/T_s) is 3. Figure 2.9(a) shows the temperature change and the corresponding entropy change versus thickness ratio when R_i/R_o is fixed to be 0.7 and Figure 2.9(b) demonstrates their changes as a function of radius ratio at T_{pz}/T_s which is set to be 3. Their insert figures are the derivative derivatives of the temperature and the entropy change with respect to thickness ratio and radius ratio respectively.

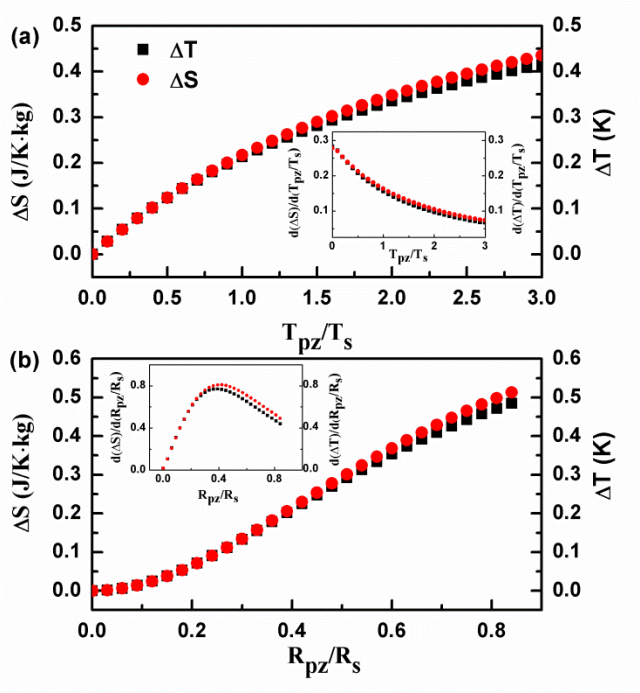

Figure 2. 9. (a) The temperature and entropy change versus thickness ratio and the insert figure is their derivatives with respect to thickness ratio at R_i/R_o=0.7 (b) The temperature and entropy change as a function of radius ratio and the insert figure is their derivatives with respect to radius ratio at T_{pz}/T_s=3.

It illustrates the rates of the changes of ΔT and ΔS are the largest at the beginning and then decrease with increment of thickness ratio. However, the rates of the changes of ΔT and ΔS become the largest when R_i/R_o is fixed to be 0.4. It clearly proves that device design influences cooling performance.

2.4 Summary

In summary, a design concept of novel way to control heat transfer process is presented in this chapter. The cooling composite is comprised by an EC layer and a substrate layer bonded together. The composites have the converse piezoelectric effect, and thus can bend upward or downward by the application of electric field. In the meantime, their temperatures change due to the electrocaloric effect. In addition, an analytical model is proposed by considering multi-physical effects, which may be more accurate to predict temperature change of the device over Indirect Method derived from Maxwell relation where only electrocaloric effect is considered. Moreover, the model sheds light on exploring the design optimization. It is noted that the model calculated the temperature change and the corresponding entropy change by only considering two layers, while it is also applicable to predict temperature change of more than two layers of a composite, like EC layers bonded on the top and bottom surfaces of substrate layer.

3.0 Optimization of Device Performance

The composite performance can be improved by a variety of factors. For example, boundary conditions with various degrees of freedom influence stress and strain in the composites and thus introduce stress-induced caloric effect. Properties of various substrate materials and electrocaloric materials have a close relation with cooling efficiency. Therefore, this chapter mainly studies and discusses factors that influence the cooling performance most and the possible explanations, which may provide a way to optimize the composite design.

3.1 Boundary Condition

Governing equation defines the general solutions of strain and stress, and boundary conditions identifies specific solutions. Here two kinds of boundary conditions were studied: fully-clamped boundary condition and simply supported boundary condition shown in Figure 3.1. These two boundary conditions had different degrees of freedom and thus the specific solutions of strain and stress were different, which resulted in different temperature change and entropy change.

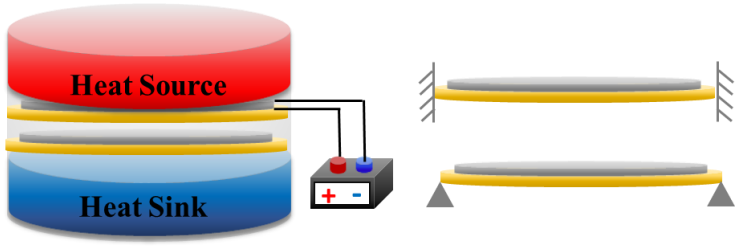

Figure 3. 1. (a) Schematic of the electrocaloric design with the composite as the cooling part and (b) two boundary conditions: fully-clamped (top) and simply-supported (bottom).

The results of temperature change and the corresponding entropy change as a function of temperature were shown in Figure 3.2 for fully-clamped and simply-supported boundary conditions respectively. The increases of the temperature change from fully-clamped to simply-supported boundary conditions were 13.0%, 14.4% and 19.5% for 20kV/cm, 10kV/cm and 5kV/cm respectively. The increases of the entropy change from fully-clamped to simply-supported boundary conditions were 15.1%, 15.1% and 23.0% respectively. The results clearly showed that the composite had better cooling performance in simply-supported boundary condition. It is reasonable that fully-clamped boundary condition has more constraints which generate stronger stress and strain and result in the favor of converse piezoelectric effect. From the viewpoint of energy conservation, the input energy is electrical energy and the output energy is mechanical energy and thermal energy. The favor of converse piezoelectric effect suppresses EC effect which leads to smaller temperature change. The other disadvantage in fully-clamped boundary condition is that constrains limit deformation and thus the composites are not able to bend enough to touch the heat source or heat sink. Figure 3.2 clearly shows that when the volume ratio of EC layer is larger in simply-supported boundary condition, it has larger temperature change while keeps the same deformation as that in fully-clamped boundary condition.

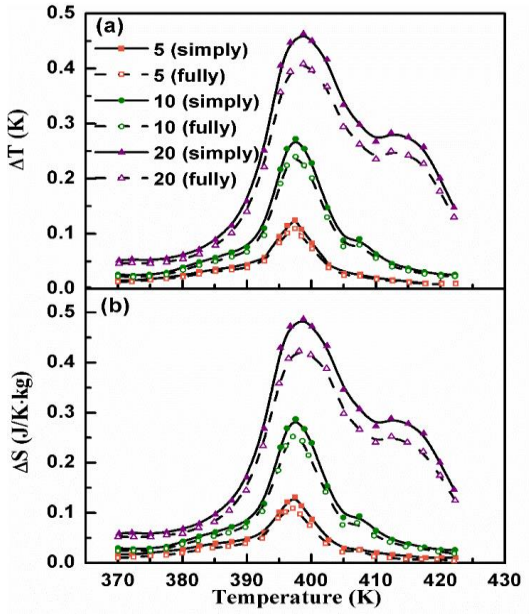

Figure 3. 2. (a) Temperature change and (b) the corresponding entropy change in both simply-supported (T_{pz}/T_s=4 and R_{pz}/R_s=0.7) and fully-clamped boundary conditions (T_{pz}/T_s=3 and R_{pz}/R_s=0.7) under different electric field (Unit is kV/cm).

3.2 Substrate Materials

Actuation mechanism is induced by discontinuous displacement between the EC layer and substrate layer. When the electric field is applied across the thickness of EC layer, converse piezoelectric effect induces elongation or shortness of the EC layer, however, the substrate layer resists to deform and therefore bending behavior occurs. In the present chapter, two typical substrate materials, copper and 2024 Aluminum were studied and compared. Copper is a prominent substrate material since it has good thermal conductivity and ductility, while 2024 Aluminum is an aluminum alloy with copper as the primary alloying element and has good fatigue

resistance and smaller density and young's modulus. Figure 3.3(a)-(b) show the temperature change and the corresponding entropy change in simply-supported boundary conditions with Copper and 2024 Aluminum as the substrate materials respectively at different electric fields, 5kV/cm, 10kV/cm and 20kV/cm.

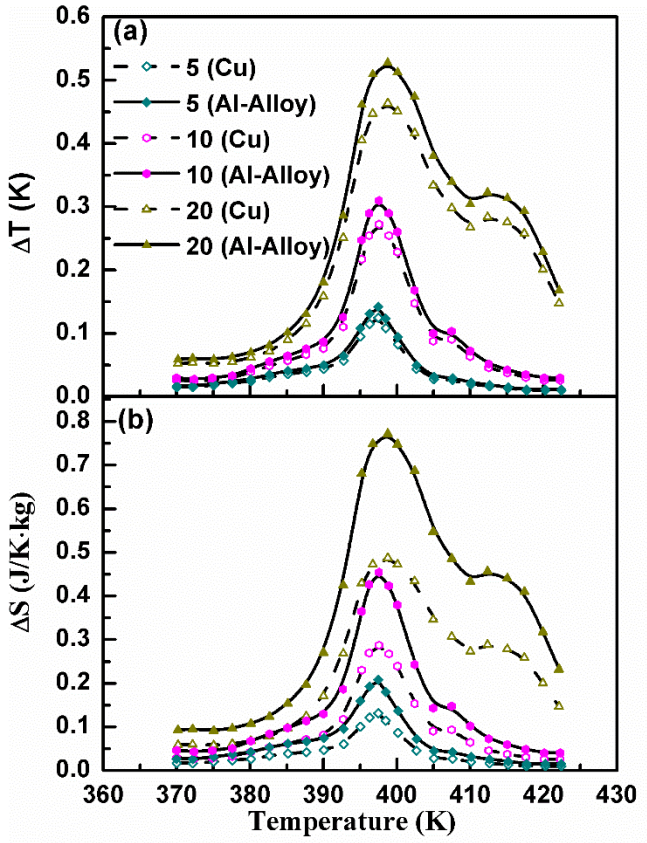

Figure 3. 3. (a) Temperature change and (b) the corresponding entropy change with different substrate materials: Cu and 2024 Aluminum.

It clearly shows that 2024 Aluminum is a better substrate material to favor electrocaloric effect than Copper. The increases of the temperature change are 0.02K, 0.03K and 0.06K under 5kV/cm, 10kV/cm and 20kV/cm respectively. The ratios of the increase are up to 13~16%. In the

corresponding entropy change, the increases are 0.07J/(K·kg), 0.16J/(K·kg) and 0.28J/(K·kg) under 5kV/cm, 10kV/cm and 20kV/cm respectively. The ratio of the increment can be up to 58%. The main reason for the large entropy increase is that the specific heat capacity of the 2024 Aluminum is much larger than that of the Copper while the density of it is smaller than that of copper.

It is clearly noted that with appropriate boundary condition and substrate material, temperature change and corresponding entropy change increase dramatically. Table 3-1 shows the temperature change and entropy change increase ratio for various conditions. The results are promising since the temperature change increase ratios are 43%, 29.8% and 28.9% for 5kV/cm, 10kV/cm and 20kV/cm respectively from fully-clamped boundary condition with Cu substrate material to simply-supported boundary condition with Al-Alloy as the substrate material. The increase ratios are much higher in entropy change with values of 95.6%, 80.9% and 83.0%. The results provide a way to improve temperature change by adjusting the composite.

Table 3. 1. Temperature change and entropy change increase ratio under different conditions.

Electric field (kV/cm)	ΔT increase ratio from fully to simply (%)	ΔT increase ratio from simply Cu to simply Al-Alloy (%)	ΔT total increase ratio (%)	ΔS increase ratio from fully to simply (%)	ΔS increase ratio from simply Cu to simply Al-Alloy (%)	ΔS total increase ratio (%)
5	19.5	18.8	43.0	23.0	62.4	95.6
10	14.4	13.9	29.8	15.1	60.9	80.9
20	13.0	14.2	28.9	15.1	58.3	83.0

3.3 Electrocaloric Materials

EC material is the core of the cooling composite which generates not only electrocaloric effect but also converse piezoelectric effect. In chapter 2, a typical lead-free material $BaTiO_3$ was studied. Here we explore the electrocaloric effect in another material. $Pb(Mg_{1/3}Nb_{2/3})O_3$-$PbTiO_3$ (PMN-PT) is an excellent relaxor ferroelectric materials [33]. Figure 3.4 illustrates the polarization as a function of temperature in 0.7PMN-0.3PT ceramic under 10kV/cm and 20kV/cm [34]. The polarization decreases smoothly with the increasing temperature and no sharp drop existence indicates second-order phase transition.

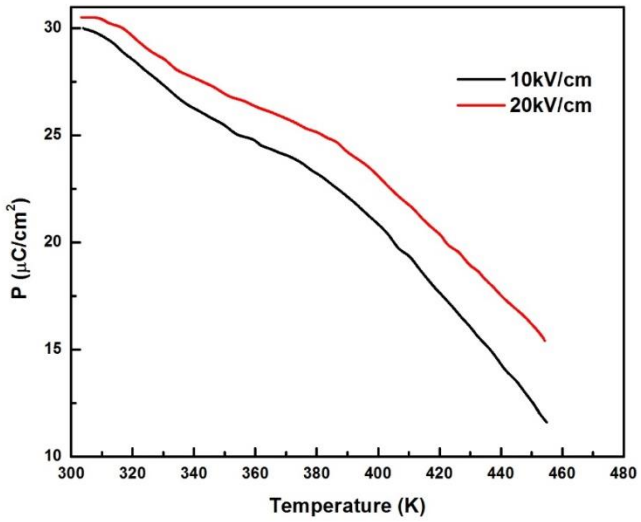

Figure 3. 4. Polarization as a function of temperature in 0.7PMN-0.3PT ceramic. Reprinted from [34], with the permission of AIP Publishing.

Figure 3.5 shows the temperature change and the corresponding entropy change in $BaTiO_3$ (BTO) and 0.70PMN-0.30PT (PMNPT) respectively. The temperature change is 0.52K in $BaTiO_3$

while the value increases to 1.22K in 0.70PMN-0.30PT when the electric field is 20kV/cm. The entropy change is 0.75J/(K·kg) in $BaTiO_3$ while in 0.70PMN-0.30PT the value is 1.5J/(K·kg). One reason of the outstanding EC effect in PMN-PT is that relaxor ferroelectrics possess a glassy polar phase, in which nanosized polar domains are distributed randomly throughout the volume of the materials. Thus, the multiple possible orientations of the polar domains might generate an enhanced EC effect.

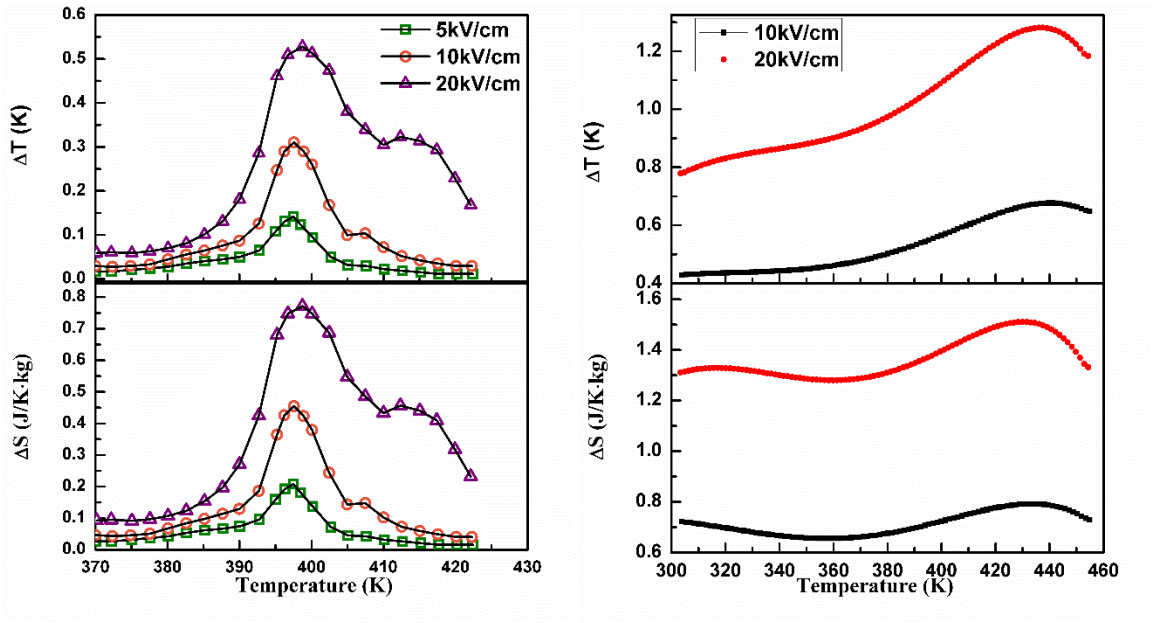

Figure 3. 5. Temperature change and the corresponding entropy change in (a) $BaTiO_3$ and (b) 0.70PMN-0.30PT.

The outstanding performance in lead-based system than lead-free-based system is due to the correct factor. From the calculation, correct factor in 0.70PMN-0.30PT is around 100 time higher than that in $BaTiO_3$. Therefore, digging into the correct factor may shed light on material selections. The key reason is piezoelectric coefficient d_{31}, where d_{31} of PMNPT is 1000 time higher

than d_{31} of BTO [35-38]. PMNPT as a relaxor ferroelectric has its outstanding properties. Relaxor ferroelectric transition is a non-egodic transition and thus there is no obvious transition temperature. Due to this property, relaxor ferroelectrics can be applied for a broad temperature range.

The temperature equation may provide a way to find the best EC material candidate. The correct factor in equation (2.17) is related with many material properties. The correct factor has linear relation with piezoelectric constant and thermal conductivity. For the mechanical property, correct factor is drawn as a function of Young's modulus and Poisson's ratio in Figure 3.6. From the result, it clearly showed that the absolute value of correct factor was larger when the Young's modulus and Poisson's ratio were larger. Higher Young's modulus means stiffer material which would generate larger stress with little deformation. In the device, the entropy change was not induced by EC effect, lattice vibration, but also the stress-induced caloric effect. The EC material had multicaloric effect due to mechanical boundary condition.

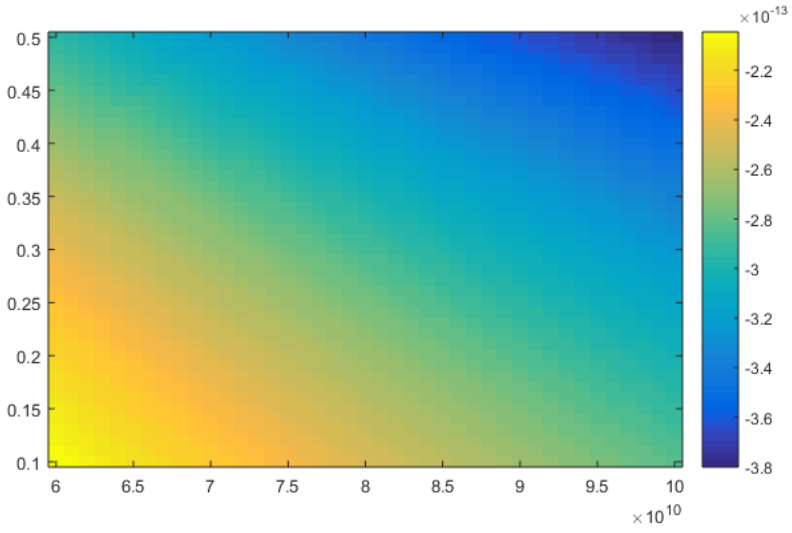

Figure 3. 6. Correct factor contour versus Young's modulus and Poisson's ratio.

3.4 Summary

In the chapter, we discussed various factors which influenced the composite performance. The fully-clamped and simply-supported boundary condition affected the EC performance by limiting the volume ratio of EC layer. Ideally, when the volume ratio of EC layer was equaled to be 1, the EC effect would be the largest. However, considering the heat transfer model of bending behavior, the volume ratio of EC layer had to be in appropriate range. Bending behavior in fully-clamped boundary condition was smaller than that in simply-supported boundary condition. Thus, the volume ratio of EC layer could not be very large. Therefore, simply-supported boundary condition would be better when the bending behavior and EC effect were considered. Two different kinds of substrate materials were studied and 2024 Aluminum alloy was proven to be better than copper, which mainly resulted from large specific heat capacity and small density. EC material played an important role in the composite which generated not only EC effect but also converse piezoelectric effect. Lead-free ferroelectric $BaTiO_3$ and lead-based relaxor ferroelectric 0.70PMN-0.30PT were studied. Due to the relaxor glassy behaviors, 0.70PMN-0.30PT was suitable EC material for a large temperature range while the $BaTiO_3$ had large temperature change only in phase transition temperature area. The correct factor was studied to explore the possible reason. The result found that higher Young's modulus had higher correct factor. The possible reason was multicaloric effect. Due to the non-free boundary condition, large stress would be induced in the EC layer and stress-induced caloric effect strengthened temperature change. In conclusion, various factors would be considered when the cooling composite was designed and the present study gave guidelines to optimize cooling performance.

4.0 Unimorph Beam Cooling Structure

Uninorph beam is a unique structure where piezoelectric layer and substrate layer are boned together. It has been widely used in energy harvesting equipment. This chapter, we explore the unimorph beam as the cooling composite. An analytical model similar to the previous model is also proposed but with some specific details. The results show that unimorph beam is definitely promising in cooling application.

4.1 Unimorph Actuators

Actuators are one of the most significant integral parts of robotic mechanisms, which requires light weight, high efficiency, long-life time and compact size [39]. Piezoelectric actuators with proper design almost satisfy all of these requirements. There are different types of piezoelectric actuators such as stack and bending types, motors, impact type, etc. Among them, flexural bending actuators generate large deflection with low weight. Therefore, bimorphs and unimorphs are more suitable [40]. These actuators consist of piezoelectric layers bonded to a purely elastic layer. Here we are mainly talk about unimorph structure.

A standard rectangular shape unimoroh actuator under activation is illustrated in Figure 4.1 [41]. The actuator consists of a single piezoelectric layer bonded to a purely elastic layer. Steel or titanium is usually chosen for the elastic layer. When a voltage is applied across the thickness of the piezoelectric layer, longitudinal and transverse strain develop. The elastic layer opposes the transverse strain which leads to a bending deformation.

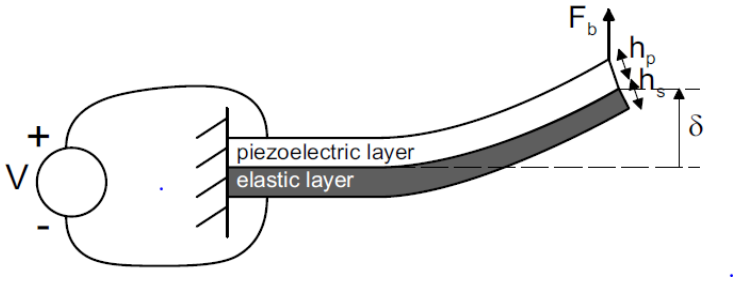

Figure 4. 1. Basic cantilevered rectangular shape unimorph actuator structure [41].

4.2 Electrocaloric Cooler Based on Unimorph Actuators

The unimorph beam is a composite which has EC layer and substrate layer boned together. The top and bottom surfaces of the EC layer are covered with silver layer which is used as an electrode. The unimorph beam, heat source and heat sink are insulated in a shell. Figure 4.2 shows the device configuration and its four working procedures [42]. At the beginning illustrated in Figure 4.2(a), the unimorph beam connects with heat source and since there is no application of electric field, heat transfer does not happen yet. When the electric field is applied across the thickness of the EC layer, the dipoles of the EC layer turn to more order state, and thus entropy decreases. In the adiabatic process, temperature of the EC layer increases. In the meantime, due to the converse piezoelectric effect, the EC layer expands while the substrate layer resists the deformation, resulting bending downward. Therefore, heat is transferred from the unimorph beam to heat sink, shown in Figure 4.2(b). In Figure 4.2(c), EC layer is not connected with voltage supplier and the unimorph beam is back to its original position. As a result, entropy increases followed by temperature decrease. Thus, heat is transferred from heat source to the unimorph beam.

As illustrated in Figure 4.2(d), after application of electric field, the unimorph beam is bent downward to connect and transfer heat to heat sink again. When the four working procedures repeat, the lowest temperature is reached in the heat source.

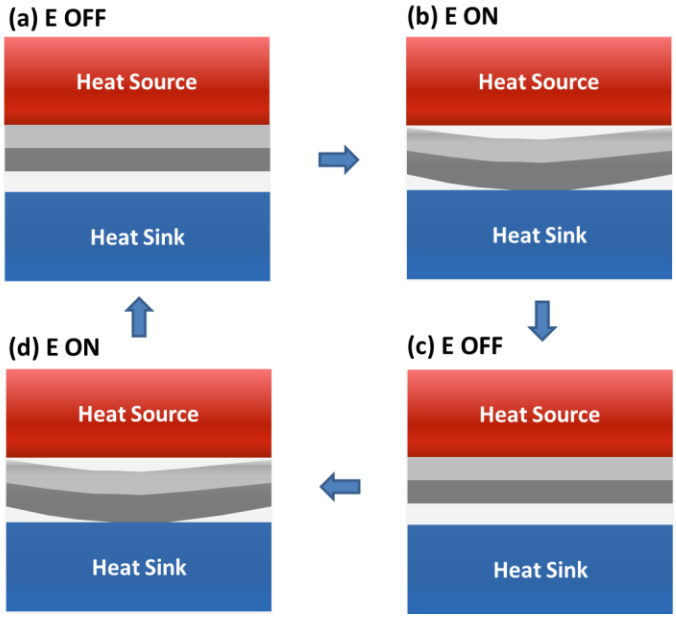

Figure 4. 2. The structure of the electrocaloric cooling device and its working procedures. (a) The electric field is off and the unimorph beam is connected with heat source. (b) The electric field is applied across the thickness of electrocaloric layer and the unimorph beam bends downward to connnect with heat sink for transferring heat. (c) The electric field is removed and heat is dumped from heat source to the unimorph beam. (d) The electric field is applied again and the unimorph beam connects to heat sink again.

It should be mentioned that the heat transfer performance depends on the size of the contact area between the unimorph beam and the heat source/heat sink. Thus, the device design can be improved by adding a piece of unbending thin metal plate which has high thermal conductivity at

the centers of the top and bottom surfaces of the beam. When the beam is bending, the metal plate contacts the heat source/heat sink to increase the contact area and thus the heat transfer process is faster.

4.3 Theoretical Analysis

The analytical model is based on beam theory and thermodynamics. There are some assumptions in the model. 1. The EC layer and the substrate layer are perfectly bonded together. 2. Properties are homogeneous inside the material. 3. The EC material is assumed to be a polycrystalline ceramic poled along the axis (z axis) normal to the surface, and therefore the in-plane strains due to the poling field are isotropic and the in-plane piezoelectric coefficients are isotropic. 4. Mechanical loss and dielectric loss are not considered. Therefore, the strain in the EC layer and substrate layer can be expressed respectively as:

$$\varepsilon_p = kz - d_{31}E_3 \tag{4.1a}$$

$$\varepsilon_m = kz \tag{4.1b}$$

where k is the curvature, which is the reciprocal of radius of bending beam; E_3 is the electric field vertical to the layer surface; d_{31} is the piezoelectric coefficient and z is the distance from the neutral plane. Subscripts p and m are used to state EC layer (piezoelectric layer) and substrate layer respectively. By using Hook's law, the stress in the EC layer and the substrate layer is written as:

$$\sigma_p = E_p(kz - d_{31}E_3) \tag{4.2a}$$

$$\sigma_m = E_m kz \tag{4.2b}$$

where E_p and E_m are the Young's modulus for the EC and substrate material respectively. Applying moment equilibrium about the center of the beam results in:

$$\int_{d-t_m}^{d} \sigma_p z\, dz + \int_{d}^{d+t_p} \sigma_m z dz = 0 \tag{4.3}$$

where d is the distance between the neutral plane and the interface of EC layer and substrate layer. t_p and t_m are the thickness of EC layer and substrate layer, respectively. By inserting equation (4.2(a)-(b)) into equation (4.3), the curvature k is expressed as:

$$k = \frac{E_p d_{31} E_3 (\frac{t_p^2}{2} + dt_p)}{E_m \left(d^2 t_m - dt_m^2 + \frac{t_m^3}{3}\right) + E_p (dt_p^2 + d^2 t_p + \frac{t_p^3}{3})} \tag{4.4}$$

Neutral plane is a surface where the stress and strain are zero. Above the neutral plane and below the neutral plane have opposite stress directions. The distance of the neutral plane inside the substrate layer away from the interface can be calculated as [43]:

$$d = \frac{E_m t_m^2 - E_p t_p^2}{2(E_p t_p + E_m t_m)} \tag{4.5}$$

The entropy changes in the EC layer and the substrate layer are derived from the piezoelectric constitutive equations respectively as:

$$ds_p = \alpha_p d\sigma_p - pdE_3 + \frac{c_p \rho_p}{T} dT \tag{4.6a}$$

$$ds_m = \alpha_m d\sigma_m + \frac{c_m \rho_m}{T} dT \tag{4.6b}$$

where ρ_p, c_p and α_p are density, specific heat capacity and thermal conductivity of the EC material respectively; ρ_m, c_m and α_m are density, specific heat capacity and thermal conductivity of the substrate material respectively; p is the pyroelectric coefficient, which is equal to the derivative of polarization with respect to temperature ($-\partial P/\partial T$). Since the entropy change is an extensive property, the entropy change in the EC layer is derived by integrating equation (4.6(a)) through the volume of the EC layer and the entropy change in the substrate layer is derived by integrating equation (4.6(b)) through the volume of the substrate layer. Thus, the total entropy change is calculated by summing them together. In an adiabatic process, the total entropy change is zero so that the temperature change is derived as:

$$\Delta T = -\int_0^{E_3} \frac{T\left(A + \omega_p\left(\frac{\partial P}{\partial T}\right)_E\right)}{\overline{\rho c}} dE \tag{4.7}$$

where $\overline{\rho c} = \omega_p c_p \rho_p + \omega_m c_m \rho_m$ is the average density timing heat capacity of the unimorph beam; ω_p and ω_m are the volume ratio of EC layer and substrate layer respectively; $A = [E_p k\left(dt_p + \frac{t_p^2}{2}\right)/E_3 + \alpha_m E_m k\left(dt_m - \frac{t_m^2}{2}\right)/E_3 - \alpha_p E_p d_{31} t_p]/(t_p + t_m)$ is a factor derived from electrical-thermal-mechanical couplings in the device.

The corresponding entropy change is expressed as:

$$\Delta S = -\int_0^{E_3} \frac{\bar{c}\left(A + \omega_{pz}\left(\frac{\partial P}{\partial T}\right)_E\right)}{\overline{\rho c}} dE \tag{4.8}$$

where $\bar{c}$ is the average specific heat capacity of the beam expressed as $\bar{c} = \omega_p c_p + \omega_m c_m$.

4.4 Results and Discussion

EC material used in this work is $BaTiO_3$ ceramic which is a strong EC lead-free alternative due to a large latent heat and a sharp phase transition. Properties of $BaTiO_3$ ceramic are reported as: density ρ_p =6020kg/m^3, heat capacity c_p=434J/(kg·K), thermal expansion coefficient α_p =6.17×10^{-6}K^{-1}, piezoelectric coefficient d_{31}=2×10^{-11}m/V, and Young's modulus E_p=6.7×10^{10}N/m^2. For the substrate layer, copper is used as it is one of the best substrate materials

for high thermal conductivity and ductility. Its properties are listed as: density ρ_m=8920kg/m^3, heat capacity c_m=390J/(kg·K), thermal expansion coefficient α_m =17.7×10^{-6}K^{-1}, and Young's modulus E_m=11×10^{10}N/m^2. With the same width and length, the thickness of the substrate layer is fixed to be 0.003 m, while the thickness of the EC layer varies due to different study purposes.

Bending behavior is one of the main features in the unimorph beam, which is resulted from the converse piezoelectric effect in the EC layer and the resistance of deformation in the substrate layer. In order to have enough bending deformation, the neutral plane is restricted inside the substrate layer. Figure 4.3 shows the location of the neutral plane varies with the thickness of the EC layer. Insert figure illustrates where the location of neutral plane is. The result displays that with the increase of the EC layer thickness, the neutral plane is closer to the interface. When the thickness of the EC layer is 0.0039m, which is 1.3 times of the thickness of the substrate layer, the neutral plane coincides with the interface. Therefore, the maximum thickness of the EC layer is 0.0039m.

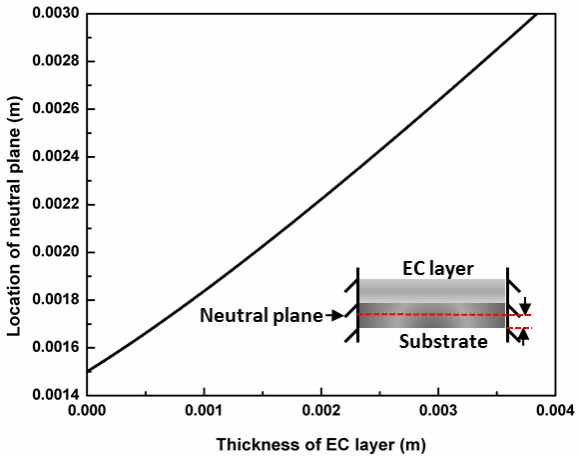

Figure 4. 3. Location of neutral plane as a function of the thickness of the EC layer.

The temperature change is significant to define the device cooling performance. Equation (4.7) is different from a commonly used indirect method derived from Maxwell equation. The indirect method considers only electric-thermal coupling in the EC material, while the analytical model in this work includes electric-thermal-mechanical couplings in the viewpoint of the device. From equation (4.7), it indicates not only electrical field and material properties but also the device dimensions influence the cooling performance. Figure 4.4 illustrates the temperature change and corresponding entropy change increase with the increase of the thickness of the EC layer when the electric field is 20kV/cm and working temperature is 397K. The thickness increasing of the EC layer means that the volume ratio of the EC layer to the substrate layer increases as well, which favors the electrocaloric effect. Thus, considering the bending behavior and electrocaloric effect, the optimal thickness of the EC layer is 0.0039m.

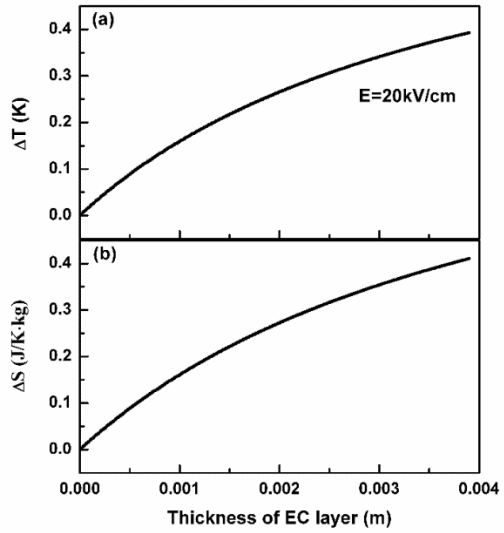

Figure 4. 4. (a) The temperature change and (b) the corresponding entropy change versus the thickness of the EC layer with an electric field of 20kV/cm at working temperature 390K.

Figure 4.5 illustrates the temperature change and the corresponding entropy change calculated from equation (4.7) and equation (4.8) with the electric field of 5kV/cm, 10kV/cm and 20kV/cm when the thicknesses of the EC layer and the substrate layer are 0.0039m and 0.003m respectively. The maximum temperature change occurs around the phase transition temperature, which has good agreement with previous results. It also shows that the temperature change and the corresponding entropy change decrease when the temperature is away from the phase transition temperature. Therefore, the solid-state electrocaloric device performs best with 0.39 K of the temperature span and 0.41J/K·kg of the entropy difference when the working temperature is 397K. From Figure 4.5, it is also obvious that the temperature change and the entropy change increase with the increase of the electric field.

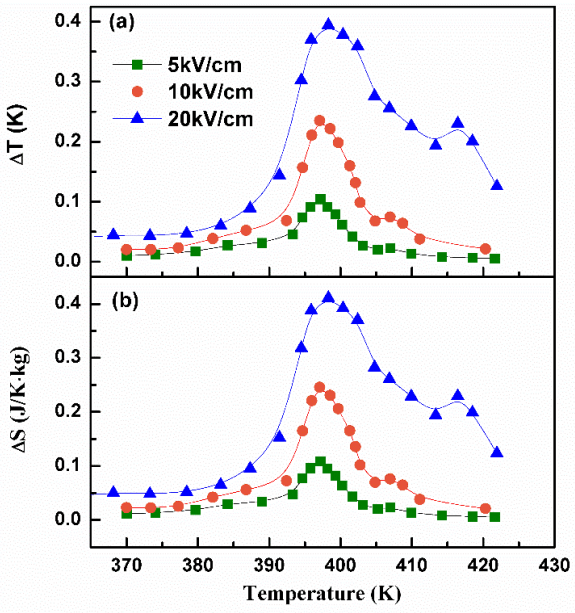

Figure 4. 5. (a) The temperature change and (b) corresponding entropy change as a function of temperature with the electric field of 5kV/cm, 10kV/cm and 20kV/cm. The thicknesses of the EC layer and the substrate layer are 0.0039m and 0.003m respectively.

4.5 Summary

In summary, the usage of unimorph beam structure created a new solid-state electrocaloric cooling composite, with bending behavior to control heat transfer process and electrocaloric effect for cooling purpose. An analytical model was proposed as well to predict the temperature change and the corresponding entropy change in the viewpoint of the device. Electrical-thermal-mechanical couplings were considered in the model. The optimization of the unimorph beam was studied with the result of the thickness of the EC layer to be 0.0039m when the substrate layer was 0.003m. The results also showed that the working temperature should be around the phase transition temperature and larger electrical field would induce larger temperature change.

5.0 Conclusion

This Ph.D. dissertation mainly focused on exploring a new and smart way to control heat transfer process in the electrocaloric based solid-state cooling device. First, a cooling composite based on electrocaloric effect and converse piezoelectric effect was developed in chapter 2. The cooling composite can bend to connect heat source or heat sink for transferring heat due to the multi-physical couplings. An analytical model based on plate theory and thermodynamics was proposed in chapter 2 as well. The equations accurately showed that temperature change was a combined result from thermal-electric-mechanical couplings. Typical lead-free $BaTiO_3$ perovskite ferroelectric was studied and the results clearly illustrated that the temperature change and corresponding entropy change were related with electric field, working temperature, thickness ratio and radius ratio of EC layer to substrate layer. In chapter 3, more thorough works were studied on improving the cooling composite performance. The results showed that simply-supported boundary was better than fully-clamped boundary condition in improving cooling performance. Two different kinds of EC materials were compared: One was lead-free $BaTiO_3$ and the other was relaxor ferroelectric PMNPT. The results illustrated that they both had good performance as cooling materials. However, $BaTiO_3$ worked best around the phase transition temperature, while PMNPT had a wide temperature range to perform electrocaloric cooling. The reason was mainly caused from the relaxation property. In chapter 4, we studied a new cooling component configuration, which was a unimorph beam. Unimorph beam has been widely used in energy harvesting devices due to the converse piezoelectric effect. Possible application on cooling had not been explored yet until we saw the potential application and the results clearly showed that unimorph beam was applicable to control heat transfer process.

6.0 Future Works

Based on the research conducted in this dissertation, following works could be recommended as future works.

6.1 Smart Solid-state Cooling Composite

Requirement for electronic cooling has been an urgent issue. The main reason is that cooling efficiency highly influences the device performance. Researches in electrocaloric cooling technology provide a promising future in solid-state cooling. We have done some research works on the design and theoretical analysis of a novel heat transfer controlling method. In order to highly improve the cooling performance, integrating shape memory materials may provide a new approach [44]. Shape memory material is very unique that remembers its original shape and that when deformed returns to its pre-deformed shape by heating. In the meantime, it may also increase the temperature change since shape memory material also has ferroelastic domain orientation, which results in temperature change under an adiabatic condition. If the shape memory alloy and electrocaloric material are bonded together, the cooling efficiency is increased by an electrostatic actuation mechanism and the improved thermal transfer contact.

6.2 Heat transfer Modeling

Modeling has been widely used in industry and academy due to its efficiency and cost reduction. It provides a visual way to explain heat transfer process. Many groups have tried to use simulation to explain the electrocaloric cooling process and provides details of how to improve the device performance [19, 45]. Since our device design is a combination of thermal-electro-mechanical couplings, it is better to visualize the heat transfer process. In the meantime, by adjusting the parameters in the simulation software, it directly shows the important results like temperature change, heat flux, heat generation, etc.

Appendix A Matlab Code

Constant equations can be expressed as a matrix expression in the eight non-zero constants as:

$$\begin{bmatrix} R_0^2 & \log(R_0) & 1 & 0 & 0 & 0 & 0 & 0 \\ 2R_0 & \frac{1}{R_0} & 0 & 0 & 0 & 0 & 0 & 0 \\ 0 & 0 & 0 & R_0 & \frac{1}{R_0} & 0 & 0 & 0 \\ R_i^2 & \log(R_i) & 1 & 0 & 0 & -R_i^2 & -1 & 0 \\ 2R_i & \frac{1}{R_i} & 0 & 0 & 0 & -2R_i & 0 & 0 \\ 0 & 0 & 0 & R_i & \frac{1}{R_i} & 0 & 0 & -R_i \\ -2(D_{11}^{ext}+D_{12}^{ext}) & \frac{D_{11}^{ext}-D_{12}^{ext}}{R_i^2} & 0 & B_{11}^{ext}+B_{12}^{ext} & -\frac{B_{11}^{ext}-B_{12}^{ext}}{R_i^2} & 2\left(D_{11}^{int}+D_{12}^{int}\right) & 0 & -\left(B_{11}^{int}+B_{12}^{int}\right) \\ 2(B_{11}^{ext}+B_{12}^{ext}) & -\frac{B_{11}^{ext}-B_{12}^{ext}}{R_i^2} & 0 & -(A_{11}^{ext}+A_{12}^{ext}) & \frac{A_{11}^{ext}-A_{12}^{ext}}{R_i^2} & -2\left(B_{11}^{int}+B_{12}^{int}\right) & 0 & A_{11}^{int}+A_{12}^{int} \end{bmatrix}$$

$$\times \begin{Bmatrix} c_1 \\ c_2 \\ c_4 \\ c_5 \\ c_6 \\ c_7 \\ c_{10} \\ c_{11} \end{Bmatrix} = \begin{Bmatrix} 0 \\ 0 \\ 0 \\ 0 \\ 0 \\ 0 \\ -M_r^p \\ N_r^p \end{Bmatrix}$$

%%%This code is to calculate c1-c12 as functions of b and c

```
%X=A\B
%Ri=b*Ro; Tpz=c*Ts
syms Ro Ts Epz Es Vpz Vs d31 Ef b c

A=[Ro*Ro,log(Ro),1,0,0,0,0,0;2*Ro,1/Ro,0,0,0,0,0,0;0,0,0,Ro,1/Ro,0,0,0;b^2*Ro^2,log(b*Ro),
1,0,0,-b^2*Ro^2,-1,0;2*b*Ro,1/(b*Ro),0,0,0,-2*b*Ro,0,0;0,0,0,b*Ro,1/(b*Ro),0,0,-b*Ro;-
Es*(Ts^3)/(6*(1-Vs)),(Es*Ts^3)/(12*(1+Vs)*(b^2*Ro^2)),0,0,0,(Es*(Ts^3))/(6*(1-
Vs))+(Epz*(6*c^2*Ts^3+3*c*Ts^3+4*c^3*Ts^3))/(6*(1-Vpz)),0,-
(Epz*(c^2*Ts^2+c*Ts^2))/(2*(1-Vpz));0,0,0,(Es*Ts)/(1-Vs),(Es*Ts)/((1+Vs)*b^2*Ro^2),-
(Epz*(c^2*Ts^2+c*Ts^2))/(1-Vpz),0,(Es*Ts)/(1-Vs)+(Epz*c*Ts)/(1-Vpz)];
```

```
B=[0,0,0,0,0,0,0,0;0,0,0,0,0,0,0,0;0,0,0,0,0,0,0,0;0,0,0,0,0,0,0,0;0,0,0,0,0,0,0,0;0,0,0,0,0,0,0,0;(-
Epz*(c^2*Ts^2+c*Ts^2)*d31*Ef)/(2*(1-Vpz)),0,0,0,0,0,0,0;(Epz*c*Ts*d31*Ef)/(1-
Vpz),0,0,0,0,0,0,0];
A=subs(A,{Ro,Ts,Epz,Es,Vpz,Vs,d31},{0.0127,0.0001,6.7e+10,11e+10,0.23,0.34,20e-12});
B=subs(B,{Ro,Ts,Epz,Es,Vpz,Vs,d31},{0.0127,0.0001,6.7e+10,11e+10,0.23,0.34,20e-12});
```

%%%This code is to calculate DeltaT and DeltaS

```
%Dementional properties
%Ri=b*Ro; Tpz=c*Ts
%b=0.6; %Radio ratio change
%Material properties for BCTO (unchange)
Epz=6.7e+10;
Es=11e+10;
Vpz=0.23;
Vs=0.34;
Dpz=6020;
Ds=8920;
Cpz=434;
Cs=390;
ap=6.17e-6;
as=17.7e-6;
d31=20e-12;
%Demensions (unchange)
Ro=0.0127;
Ts=0.0001;
%External conditions (change)
T=397; %(curie temp)
Ef=2000000; %external field
DpDT=-0.26;%change
%Results from C_Constant
C=0:0.01:3;
B=0:0.01:0.85;
[c,b]=meshgrid(C,B);

c5=-(1291714128775658917690297845072911742187 5*b.^2.*c.*(-
37843187366474412168705330429080457966754003125 00*b.^2.*c.^3 -
41287304787069154549585241404687 50*b.^2.*c.^2 -
20643652393534577274792620702343 75*b.^2.*c +
37843187366474412168705330429080457966754003125 00*c.^3 +
41287304787069154549585241404687 50*c.^2 + 20643652393534577274792620702343 75*c +
10818762260408879644604264527950251645342742216704))./(9007199254740992*(2713528
27980628321996518599838442969097210317001927203810198604375654400000000000000*
b.^4.*c.^4 +
41580433342305218786543432600710409847672649935743531402145465322590479052246 0
```

9375000*b.^4.*c.^3 +
623706500134578252193280194277814291773209051551654189311422258963726305783691
4062500*b.^4.*c.^2 +
311853250067289118695422273455696681901134351404702399225521199263080432891845
7031250*b.^4.*c -
542705655961256643993037199676885938194420634003854407620397208751308800000000
000000*b.^2.*c.^4 -
726106074783538897868344892142479037846588604171632065082520070292422625783691
4062500*b.^2.*c.^3 -
108915911217530828759277474874803484488612151128845053418226066368837217867553
71093750*b.^2.*c.^2 -
622154991427775781115049582567151896092757494737227546560076175490684610556840
5546875*b.^2.*c -
297179528417381475540830873244697116801081429027139879346377566291609386624016
5019648*b.^2 +
271352827980628321996518599838442969097210317001927203810198604375654400000000
000000*c.^4 +
310301741360486710002910566135374939369862104814196751061065417066517835261230
4687500*c.^3 +
465452612040730035399494554470220553112912459736796344870838404724645872891845
7031250*c.^2 +
310301741360486662419627309111455214191623143332525147334554976227604177664994
8515625*c +
221775767475657814086404782552250071554779955938092256717872770401974566487621
9990016));
c7=-
(559473682025957268724610254147204898334960937 5*(356738996766259002678440821394
2806*b.^4.*c.^2 + 35673899676625900267844082139 42806*b.^4.*c -
622962128681377657214592320370563 3*b.^2.*c.^2 -
622962128681377657214592320370563 3*b.^2.*c +
266223131915118654536151498976282 7*c.^2 +
266223131915118654536151498976282 7*c))./(32*(271352827980628321996518599838442969
0972103170019272038101986043756544000000000000000*b.^4.*c.^4 +
415804333423052187865434326007104098476726499357435314021454653225904790522460
9375000*b.^4.*c.^3 +
623706500134578252193280194277814291773209051551654189311422258963726305783691
4062500*b.^4.*c.^2 +
311853250067289118695422273455696681901134351404702399225521199263080432891845
7031250*b.^4.*c -
542705655961256643993037199676885938194420634003854407620397208751308800000000
000000*b.^2.*c.^4 -
726106074783538897868344892142479037846588604171632065082520070292422625783691
4062500*b.^2.*c.^3 -
108915911217530828759277474874803484488612151128845053418226066368837217867553
71093750*b.^2.*c.^2 -
622154991427775781115049582567151896092757494737227546560076175490684610556840

5546875*b.^2.*c -
297179528417381475540830873244697116801081429027139879346377566291609386624016
5019648*b.^2 +
271352827980628321996518599838442969097210317001927203810198604375654400000000
000000*c.^4 +
310301741360486710002910566135374939369862104814196751061065417066517835261230
4687500*c.^3 +
465452612040730035399494554470220553112912459736796344870838404724645872891845
7031250*c.^2 +
310301741360486662419627309111455214191623143332525147334554976227604177664994
8515625*c +
221775767475657814086404782552250071554779955938092256717872770401974566487621
9990016));
c11=-(129171412877565891769029784507291174218 75*c.*(b.^2 - 1).*(-
378431873664744121687053304290804579667540031 2500*b.^2.*c.^3 -
412873047870691545495852414046875 0*b.^2.*c.^2 -
206436523935345772747926207023437 5*b.^2.*c +
378431873664744121687053304290804579667540031 2500*c.^3 +
412873047870691545495852414046875 0*c.^2 + 206436523935345772747926207023437 5*c +
108187622604088796446042645279502516453427422167 04)).*(9007199254740992*(271352
827980628321996518599838442969097210317001927203810198604375654400000000000000*
b.^4.*c.^4 +
415804333423052187865434326007104098476726499357435314021454653225904790522460
9375000*b.^4.*c.^3 +
623706500134578252193280194277814291773209051551654189311422258963726305783691
4062500*b.^4.*c.^2 +
311853250067289118695422273455696681901134351404702399225521199263080432891845
7031250*b.^4.*c -
542705655961256643993037199676885938194420634003854407620397208751308800000000
000000*b.^2.*c.^4 -
726106074783538897868344892142479037846588604171632065082520070292422625783691
4062500*b.^2.*c.^3 -
108915911217530828759277474874803484488612151128845053418226066368837217867553
71093750*b.^2.*c.^2 -
622154991427775781115049582567151896092757494737227546560076175490684610556840
5546875*b.^2.*c -
297179528417381475540830873244697116801081429027139879346377566291609386624016
5019648*b.^2 +
271352827980628321996518599838442969097210317001927203810198604375654400000000
000000*c.^4 +
310301741360486710002910566135374939369862104814196751061065417066517835261230
4687500*c.^3 +
465452612040730035399494554470220553112912459736796344870838404724645872891845
7031250*c.^2 +
310301741360486662419627309111455214191623143332525147334554976227604177664994
8515625*c +

22177576747565781408640478255225007155477995593809225671787277040197456648762199990016));

%Results
A=2*(pi*b.^2*Ro^2*ap*Epz.*c*Ts.*c11/(1-Vpz)-pi*b.^2*Ro^2*ap*Epz.*c*Ts.*(c*Ts+Ts).*c7/(1-Vpz)-pi*b.^2*Ro^2*ap*Epz.*c*Ts*d31/(1-Vpz)+pi*b.^2*Ro^2*as*Es*Ts.*c11/(1-Vs)+pi*(Ro*Ro-b.^2*Ro^2)*as*Es*Ts.*c5/(1-Vs));
C=(pi*b.^2*Ro^2*Cpz.*c*Ts*Dpz+pi*Ro*Ro*Cs*Ts*Ds);
F=pi*b.^2*Ro^2.*c*Ts;
DeltaT=-T*(A+F*DpDT*0.01)*Ef./C;
Cav=(pi*b.^2*Ro^2*Cpz.*c*Ts+pi*Ro*Ro*Cs*Ts)./(pi*b.^2*Ro^2.*c*Ts+pi*Ro*Ro*Ts);
DeltaS=-Cav.*(A+F*DpDT*0.01)*Ef./C;
D=A./C;
E=F./C;
figure(1),mesh(c,b,DeltaT);
xlabel('c'),ylabel('b'),zlabel('DeltaT');
figure(2),mesh(c,b,D);
xlabel('c'),ylabel('b'),zlabel('D');
figure(3),mesh(c,b,E);
xlabel('c'),ylabel('b'),zlabel('E');
figure(4),mesh(c,b,DeltaS);
xlabel('c'),ylabel('b'),zlabel('DeltaS');

%%%This is to draw plate deflection
%Deflection as a function of position
%Wint=c7*r^2+c10
%Wext=c1*r^2+c2*lnr+c4
%when the device dimensitions are fixed
b=0.7;
c=1.5;
Ro=0.0127;
Ts=0.0001;
Ef=2e6;
r=0:0.001:0.009;
Wint=-(55947368202595726872461025414720489833496093754.*(3567389967662590026784408213942806*Ef*b^4*c^2 + 3567389967662590026784408213942806*Ef*b^4*c - 62296212868137765721459232037056330*Ef*b^2*c^2 - 62296212868137765721459232037056330*Ef*b^2*c + 26622313191511865453615149897628270*Ef*c^2 + 26622313191511865453615149897628270*Ef*c))/(32*(27135282798062832199651859983844296909721031700192720381019860437565440000000000000*b^4*c^4 + 4158043334230521878654343260071040984767264993574353140214546532259047905224609375000*b^4*c^3 + 623706500134578252193280194277814291773209051551654189311422258963726305783691

4062500*b^4*c^2 +
3118532500672891186954222734556966819011343514047023992255211992630804328918457031250*b^4*c -
5427056559612566439930371996768859381944206340038544076203972087513088000000000000000*b^2*c^4 -
726106074783538897868344892142479037846588604171632065082520070292422625783691
4062500*b^2*c^3 -
1089159112175308287592774748748034844886121511288450534182260663688372178675537
1093750*b^2*c^2 -
6221549914277757811150495825671518960927574947372275465600761754906846105568405546875*b^2*c -
2971795284173814755408308732446971168010814290271398793463775662916093866240165019648*b^2 +
2713528279806283219965185998384429690972103170019272038101986043756544000000000000000*c^4 +
3103017413604867100029105661353749393698621048141967510610654170665178352612304687500*c^3 +
4654526120407300353994945544702205531129124597367963448708384047246458728918457031250*c^2 +
3103017413604866624196273091114552141916231433325251473345549762276041776649948515625*c +
2217757674756578140864047825522500715547799559380922567178727704019745664876219990016))*r.^2-
(2310080260453546185538365130019908558142613 75*(1308713402971926088769830757862211492217368059597 1*Ef*b^2*c^2 -
17536759599823809864803312969972468133987583813638*Ef*b^4*c^2 +
1308713402971926088769830757862211492217368059597 1*Ef*b^2*c -
17536759599823809864803312969972468133987583813638*Ef*b^4*c +
2997405994225836934279443874590259088328174338048*Ef*b^2*c^2*log((127*b)/10000) -
4016524032262621554984824949073018351641578962944*Ef*b^4*c^2*log((127*b)/10000) +
2997405994225836934279443874590259088328174338048*Ef*b^2*c*log((127*b)/10000) -
4016524032262621554984824949073018351641578962944*Ef*b^4*c*log((127*b)/10000)))/(
4611686018427387904*(2713528279806283219965185998384429690972103170019272038101986043756544000000000000000*b^4*c^4 +
4158043334230521878654343260071040984767264993574353140214546532259047905224609375000*b^4*c^3 +
6237065001345782521932801942778142917732090515516541893114222589637263057836914062500*b^4*c^2 +
3118532500672891186954222734556966819011343514047023992255211992630804328918457031250*b^4*c -
5427056559612566439930371996768859381944206340038544076203972087513088000000000000000*b^2*c^4 -
726106074783538897868344892142479037846588604171632065082520070292422625783691
4062500*b^2*c^3 -
1089159112175308287592774748748034844886121511288450534182260663688372178675537
1093750*b^2*c^2 -

```
622154991427775781115049582567151896092757494737227546560076175490684610556840
5546875*b^2*c -
297179528417381475540830873244697116801081429027139879346377566291609386624016
5019648*b^2 +
271352827980628321996518599838442969097210317001927203810198604375654400000000
000000*c^4 +
310301741360486710002910566135374939369862104814196751061065417066517835261230
4687500*c^3 +
465452612040730035399494554470220553112912459736796344870838404724645872891845
7031250*c^2 +
310301741360486662419627309111455214191623143332525147334554976227604177664994
8515625*c +
221775767475657814086404782552250071554779955938092256717872770401974566487621
9990016));

r1=0.00889:0.001:0.0127;
Wext=(559473682025957268724610254147204898334960937 5*(-
356738996766259002678440821394280 6*Ef*b^4*c^2 -
356738996766259002678440821394280 6*Ef*b^4*c +
266223131915118654536151498976282 7*Ef*b^2*c^2 +
266223131915118654536151498976282 7*Ef*b^2*c))/(32*(271352827980628321996518599838
442969097210317001927203810198604375654400000000000000*b^4*c^4 +
415804333423052187865434326007104098476726499357435314021454653225904790522460
9375000*b^4*c^3 +
623706500134578252193280194277814291773209051551654189311422258963726305783691
4062500*b^4*c^2 +
311853250067289118695422273455696681901134351404702399225521199263080432891845
7031250*b^4*c -
542705655961256643993037199676885938194420634003854407620397208751308800000000
000000*b^2*c^4 -
726106074783538897868344892142479037846588604171632065082520070292422625783691
4062500*b^2*c^3 -
108915911217530828759277474874803484488612151128845053418226066368837217867553
71093750*b^2*c^2 -
622154991427775781115049582567151896092757494737227546560076175490684610556840
5546875*b^2*c -
297179528417381475540830873244697116801081429027139879346377566291609386624016
5019648*b^2 +
271352827980628321996518599838442969097210317001927203810198604375654400000000
000000*c^4 +
310301741360486710002910566135374939369862104814196751061065417066517835261230
4687500*c^3 +
465452612040730035399494554470220553112912459736796344870838404724645872891845
7031250*c^2 +
310301741360486662419627309111455214191623143332525147334554976227604177664994
8515625*c +
```

2217757674756578140864047825522500715547799559380922567178727704019745664876219990016))*r1.^2-(2310080260453546185538365130019908558142613 75*(-35673899676625900267844082139428 06*Ef*b^4*c^2 - 35673899676625900267844082139428 06*Ef*b^4*c + 266223131915118654536151498976282 7*Ef*b^2*c^2 + 266223131915118654536151498976282 7*Ef*b^2*c))/(4096*(2713528279806283219965185998384429690972103170019272038101986043756544000000000000000*b^4*c^4 + 4158043334230521878654343260071040984767264993574353140214546532259047905224609375000*b^4*c^3 + 623706500134578252193280194277814291773209051551654189311422258963726305783691406250 0*b^4*c^2 + 3118532500672891186954222734556966819011343514047023992255211992630804328918457031250*b^4*c - 5427056559612566439930371996768859381944206340038544076203972087513088000000000000000*b^2*c^4 - 7261060747835388978683448921424790378465886041716320650825200702924226257836914062500*b^2*c^3 - 1089159112175308287592774748748034844886121511288450534182260663688372178675537109375 0*b^2*c^2 - 6221549914277757811150495825671518960927574947372275465600761754906846105568405546875*b^2*c - 2971795284173814755408308732446971168010814290271398793463775662916093866240165019648*b^2 + 2713528279806283219965185998384429690972103170019272038101986043756544000000000000000*c^4 + 3103017413604867100029105661353749393698621048141967510610654170665178352612304687500*c^3 + 4654526120407300353994945544702205531129124597367963448708384047246458728918457031250*c^2 + 3103017413604866624196273091114552141916231433325251473345549762276041776649948515625*c + 2217757674756578140864047825522500715547799559380922567178727704019745664876219990016))*log(r1)+(32400566444417132967461931710387822002441524869253132330487912 5*b*(35673899676625900267844082139428 06*Ef*b^3*c^2 + 35673899676625900267844082139428 06*Ef*b^3*c - 266223131915118654536151498976282 7*Ef*b*c^2 - 266223131915118654536151498976282 7*Ef*b*c))/(11805916207174113034 24*(2713528279806283219965185998384429690972103170019272038101986043756544000000000000000*b^4*c^4 + 4158043334230521878654343260071040984767264993574353140214546532259047905224609375000*b^4*c^3 + 623706500134578252193280194277814291773209051551654189311422258963726305783691406250 0*b^4*c^2 + 3118532500672891186954222734556966819011343514047023992255211992630804328918457031250*b^4*c - 542705655961256643993037199676885938194420634003854407620397208751308800000000

```
000000*b^2*c^4 -
726106074783538897868344892142479037846588604171632065082520070292422625783691
4062500*b^2*c^3 -
108915911217530828759277474874803484488612151128845053418226066368837217867553
71093750*b^2*c^2 -
622154991427775781115049582567151896092757494737227546560076175490684610556840
5546875*b^2*c -
297179528417381475540830873244697116801081429027139879346377566291609386624016
5019648*b^2 +
271352827980628321996518599838442969097210317001927203810198604375654400000000
000000*c^4 +
310301741360486710002910566135374939369862104814196751061065417066517835261230
4687500*c^3 +
465452612040730035399494554470220553112912459736796344870838404724645872891845
7031250*c^2 +
310301741360486662419627309111455214191623143332525147334554976227604177664994
8515625*c +
221775767475657814086404782552250071554779955938092256717872770401974566487621
9990016));

figure(1);
plot(r,Wint);
hold on
plot(r1,Wext);
hold off


%%%neutral plane calculation

Epz=6.7e+10;
Es=11e+10;
Vpz=0.23;
Vs=0.34;
Ts=0.0005;
%Ts=0.5*(Es*Ts^2/(1-Vs^2)+Epz*(Tpz^2+2*Tpz*Ts)/(1-Vpz^2))/(Es*Ts/(1-
Vs^2)+Epz*Tpz/(1-Vpz^2));
Tpz=solve('Ts-0.5*(Es*Ts^2/(1-Vs^2)+Epz*(Tpz^2+2*Tpz*Ts)/(1-Vpz^2))/(Es*Ts/(1-
Vs^2)+Epz*Tpz/(1-Vpz^2))=0','Tpz');

a=(Ts*(-(1.0*Epz*Es)/(- 1.0*Vpz^2*Vs^2 + Vpz^2 + Vs^2 - 1.0))^(1/2) - 1.0*Ts*Vpz^2*(-
(1.0*Epz*Es)/(- 1.0*Vpz^2*Vs^2 + Vpz^2 + Vs^2 - 1.0))^(1/2))/Epz;


%%%This is to calculate DeltaT and DeltaS with different dimension ratios
%Dementional properties
%Ri=b*Ro; Tpz=c*Ts
```

```
%Material properties for BCTO (unchange)
Epz=6.7e+10;
Es=11e+10;
Vpz=0.23;
Vs=0.34;
Dpz=6020;
Ds=8920;
Cpz=434;
Cs=390;
ap=6.17e-6;
as=17.7e-6;
d31=20e-12;
%Demensions (unchange)
Ro=0.0127;
Ts=0.0001;
%External conditions (change)
T=397;
Ef=2000000;
DpDT=-0.26;
%Results from C_Constant
c=0:0.1:3;
b=0.7;

%Results from C_constants
c5=-(1291714128775658917690297845072911742187 5*b^2*c.*(-
3784318736647441216870533042908045796675400312500*b^2*c.^3 -
4128730478706915454958524140468750*b^2*c.^2 -
2064365239353457727479262070234375*b^2*c +
3784318736647441216870533042908045796675400312500*c.^3 +
4128730478706915454958524140468750*c.^2 + 206436523935345772747926207023437 5*c +
1081876226040887964460426452795025164534274221 6704)./(9007199254740992*(2713528
279806283219965185998384429690972103170019272038101986043756544000000000000000*
b^4*c.^4 +
4158043334230521878654343260071040984767264993574353140214546532259047905224609375000*b^4*c.^3 +
6237065001345782521932801942778142917732090515516541893114222589637263057836914062500*b^4*c.^2 +
3118532500672891186954222734556966819011343514047023992255211992630804328918457031250*b^4*c -
5427056559612566439930371996768859381944206340038544076203972087513088000000000000000*b^2*c.^4 -
7261060747835388978683448921424790378465886041716320650825200702924226257836914062500*b^2*c.^3 -
1089159112175308287592774748748034844886121511288450534182260663688372178675537109375 0*b^2*c.^2 -
6221549914277757811150495825671518960927574947372275465600761754906846105568400
```

5546875*b^2*c -
29717952841738147554083087324469711680108142902713987934637756629160938662401650196 48*b^2 +
27135282798062832199651859983844296909721031700192720381019860437565440000000000000 0*c.^4 +
31030174136048671000291056613537493936986210481419675106106541706651783526123046875 00*c.^3 +
46545261204073003539949455447022055311291245973679634487083840472464587289184570312 50*c.^2 +
31030174136048666241962730911145521419162314333252514733455497622760417766499485156 25*c +
22177576747565781408640478255225007155477995593809225671787277040197456648762199900 16));
c7=-
(55947368202595726872461025414720489833496093 75*(35673899676625900267844082139428 06*b^4*c.^2 + 35673899676625900267844082139428 06*b^4*c -
62296212868137765721459232037056 33*b^2*c.^2 -
62296212868137765721459232037056 33*b^2*c +
26622313191511865453615149897628 27*c.^2 +
26622313191511865453615149897628 27*c))./(32*(27135282798062832199651859983844296909721031700192720381019860437565440000000000000 0*b^4*c.^4 +
41580433342305218786543432600710409847672649935743531402145465322590479052246093750 00*b^4*c.^3 +
62370650013457825219328019427781429177320905155165418931142225896372630578369140625 00*b^4*c.^2 +
31185325006728911869542227345569668190113435140470239922552119926308043289184570312 50*b^4*c -
54270565596125664399303719967688593819442063400385440762039720875130880000000000000 0*b^2*c.^4 -
72610607478353889786834489214247903784658860417163206508252007029242262578369140625 00*b^2*c.^3 -
10891591121753082875927747487480348448861215112884505341822606636883721786755371093750*b^2*c.^2 -
62215499142777578111504958256715189609275749473722754656007617549068461055684055468 75*b^2*c -
29717952841738147554083087324469711680108142902713987934637756629160938662401650196 48*b^2 +
27135282798062832199651859983844296909721031700192720381019860437565440000000000000 0*c.^4 +
31030174136048671000291056613537493936986210481419675106106541706651783526123046875 00*c.^3 +
46545261204073003539949455447022055311291245973679634487083840472464587289184570312 50*c.^2 +
31030174136048666241962730911145521419162314333252514733455497622760417766499485156 25*c +

```
2217757674756578140864047825522500715547799559380922567178727704019745664876219990016));
c11=-(1291714128775658917690297845072911742187 5*c*(b^2 - 1).*(-3784318736647441216870533042908045796675400312500*b^2*c.^3 - 4128730478706915454958524140468750*b^2*c.^2 - 2064365239353457727479262070234375*b^2*c + 3784318736647441216870533042908045796675400312500*c.^3 + 4128730478706915454958524140468750*c.^2 + 2064365239353457727479262070234375*c + 1081876226040887964460426452795025164534274221 6704)).*(9007199254740992*(271352827980628321996518599838442969097210317001927203810198604375654400000000000000*b^4*c.^4 + 4158043334230521878654343260071040984767264993574353140214546532259047905224609375000*b^4*c.^3 + 6237065001345782521932801942778142917732090515516541893114222589637263057836914062500*b^4*c.^2 + 3118532500672891186954222734556966819011343514047023992255211992630804328918457031250*b^4*c - 5427056559612566439930371996768859381944206340038544076203972087513088000000000000000*b^2*c.^4 - 7261060747835388978683448921424790378465886041716320650825200702924226257836914062500*b^2*c.^3 - 1089159112175308287592774748748034844886121511288450534182260663688372178675537109375 0*b^2*c.^2 - 6221549914277757811150495825671518960927574947372275465600761754906846105568405546875*b^2*c - 2971795284173814755408308732446971168010814290271398793463775662916093866240165019648*b^2 + 2713528279806283219965185998384429690972103170019272038101986043756544000000000000000*c.^4 + 3103017413604867100029105661353749393698621048141967510610654170665178352612304687500*c.^3 + 4654526120407300353994945544702205531129124597367963448708384047246458728918457031250*c.^2 + 3103017413604866624196273091114552141916231433325251473345549762276041776649948515625*c + 2217757674756578140864047825522500715547799559380922567178727704019745664876219990016));


%Results
A=2*(pi*b^2*Ro^2*ap*Epz.*c*Ts.*c11/(1-Vpz)-pi*b^2*Ro^2*ap*Epz.*c*Ts.*(c*Ts+Ts).*c7/(1-Vpz)-pi*b^2*Ro^2*ap*Epz.*c*Ts*d31/(1-Vpz)+pi*b^2*Ro^2*as*Es*Ts.*c11/(1-Vs)+pi*(Ro*Ro-b^2*Ro^2)*as*Es*Ts.*c5/(1-Vs));
C=(pi*b^2*Ro^2*Cpz*c*Ts*Dpz+pi*Ro*Ro*Cs*Ts*Ds);
F=pi*b^2*Ro^2*c*Ts;
DeltaT=-T*(A+F*DpDT*0.01)*Ef./C;
```

```
Cav=(pi*b^2*Ro^2*Cpz*c*Ts+pi*Ro*Ro*Cs*Ts)./(pi*b^2*Ro^2*c*Ts+pi*Ro*Ro*Ts);
DeltaS=-Cav.*(A+F*DpDT*0.01)*Ef./C;


%b fixed, c change
figure(1)
plot(c,DeltaT,'red');
hold on
plot(c,DeltaS,'black');
hold off
```

Bibliography

[1] W. R. Cline, *The economics of global warming*. Washington: Institute for International Economics, 1992.

[2] G. E. Moore, "Gramming more components onto integrated circuits," *Electronics,* vol. 38, pp. 114-117, 1965.

[3] O. V. Pakhomov, S. F. Karmanenko, A. A. Semenov, A. S. Starkov, and A. V. Es'kov, "Thermodynamic estimation of cooling efficiency using an electrocaloric solid-state line," *Technical Physics,* journal article vol. 55, no. 8, pp. 1155-1160, August 01 2010.

[4] C. Zimm *et al.*, "Description and Performance of a Near-Room Temperature Magnetic Refrigerator," in *Advances in Cryogenic Engineering*, P. Kittel, Ed. Boston, MA: Springer US, 1998, pp. 1759-1766.

[5] R. A. Taylor and G. L. Solbrekken, "Comprehensive system-level optimization of thermoelectric devices for electronic cooling applications," *IEEE Transactions on Components and Packaging Technologies,* vol. 31, no. 1, pp. 23-31, 2008.

[6] A. Smith, "Who discovered the magnetocaloric effect?," *The European Physical Journal H,* vol. 38, no. 4, pp. 507-517, 2013.

[7] J. a. K. A. Gschneidner and V. K. Pecharsky, "Magnetocaloric Materials," *Annual Review of Materials Science,* vol. 30, no. 1, pp. 387-429, 2000.

[8] B. Neese, B. Chu, S.-G. Lu, Y. Wang, E. Furman, and Q. M. Zhang, "Large Electrocaloric Effect in Ferroelectric Polymers Near Room Temperature," *Science,* vol. 321, pp. 821-823, 2008-08-08 00:00:00 2008.

[9] W. Thomson, "II. On the thermoelastic, thermomagnetic, and pyroelectric properties of matter," *The London, Edinburgh, and Dublin Philosophical Magazine and Journal of Science,* vol. 5, no. 28, pp. 4-27, 1878/01/01 1878.

[10] J. F. Hautzenlaub, "Electric and dielectric behaviour of potassium dihydrogen phosphate," *PhD thesis, Massachusetts Institute of Technology,* 1943.

[11] A. I. Karchevskii, "Electrocaloric effect in polycrystalline BaTiO3," *Soviet Physics -Solid State,* vol. 3, no. 2249, 1962.

[12] R. Radebaugh, W. N. Lawless, J. D. Siegwarth, and A. J. Morrow, *Feasibility of electrocaloric refrigeration for the 4–15 K temperature range*. 1979, pp. 187-208.

[13] P. D. Thacher, "Electrocaloric Effects in Some Ferroelectric and Antiferroelectric Pb(Zr, Ti)O3 Compounds," *Journal of Applied Physics,* vol. 39, no. 4, pp. 1996-2002, 1968.

[14] A. S. Mischenko, Q. Zhang, J. F. Scott, R. W. Whatmore, and N. D. Mathur, "Giant Electrocaloric Effect in Thin-Film PbZr0.95Ti0.05O3," *Science,* vol. 311, no. 5765, pp. 1270-1271, 2006.

[15] A.-K. Axelsson, F. L. Goupil, L. J. Dunne, G. Manos, M. Valant, and N. M. Alford, "Microscopic interpretation of sign reversal in the electrocaloric effect in a ferroelectric PbMg1/3Nb2/3O3-30PbTiO3 single crystal," *Applied Physics Letters,* vol. 102, no. 10, p. 102902, 2013.

[16] B. R. Zdravko Kutnjak, Rasa Pirc, "Electrocaloric Effect: Theory, Measurements, and Applications," in *Wiley Encyclopedia of Electrical and Electronics Engineering,* 2015, pp. 1-19.

[17] P. Blumenthal and A. Raatz, "Classification of electrocaloric cooling device types," *EPL (Europhysics Letters),* vol. 115, no. 1, 2016.

[18] Y. V. Sinyavsky and V. M. Brodyansky, "Experimental testing of electrocaloric cooling with transparent ferroelectric ceramic as a working body," *Ferroelectrics,* vol. 131, no. 1, pp. 321-325, 1992/06/01 1992.

[19] D. Guo *et al.*, "Design and modeling of a fluid-based micro-scale electrocaloric refrigeration system," *International Journal of Heat and Mass Transfer,* vol. 72, pp. 559-564, 2014/05/01/ 2014.

[20] B. Yu, M. Liu, P. W. Egolf, and A. Kitanovski, "A review of magnetic refrigerator and heat pump prototypes built before the year 2010," *International Journal of Refrigeration,* vol. 33, no. 6, pp. 1029-1060, 2010/09/01/ 2010.

[21] H. Gu *et al.*, "A chip scale electrocaloric effect based cooling device," *Applied Physics Letters,* vol. 102, no. 12, 2013.

[22] L. Xinyu, G. Haiming, Q. Xiaoshi, and Q. Zhang, "Compact cooling devices based on giant electrocaloric effect dielectrics," in *13th InterSociety Conference on Thermal and Thermomechanical Phenomena in Electronic Systems*, 2012, pp. 934-937.

[23] H. Gu, B. Craven, X. Qian, X. Li, A. Cheng, and Q. M. Zhang, "Simulation of chip-size electrocaloric refrigerator with high cooling-power density," *Applied Physics Letters,* vol. 102, no. 11, p. 112901, 2013.

[24] H. Gu, X.-S. Qian, H.-J. Ye, and Q. M. Zhang, "An electrocaloric refrigerator without external regenerator," *Applied Physics Letters,* vol. 105, no. 16, p. 162905, 2014.

[25] M. Ožbolt, A. Kitanovski, J. Tušek, and A. Poredoš, "Electrocaloric refrigeration: Thermodynamics, state of the art and future perspectives," *International Journal of Refrigeration,* vol. 40, pp. 174-188, 2014/04/01/ 2014.

[26] R. I. Epstein and K. J. Malloy, "Electrocaloric devices based on thin-film heat switches," *Journal of Applied Physics,* vol. 106, no. 6, p. 064509, 2009.

[27] Z. Sun, Q.-M. Wang, and W. S. Slaughter, "A solid-state refrigeration based on electrocaloric effect: Device and its analytical model," *Journal of Applied Physics,* vol. 124, no. 6, p. 064503, 2018.

[28] M. Deshpande and L. Saggere, "An analytical model and working equations for static deflections of a circular multi-layered diaphragm-type piezoelectric actuator," *Sensors and Actuators A: Physical,* vol. 136, no. 2, pp. 673-689, 2007.

[29] R. M. Jones, *Mechanics of composite materials*. CRC press, 1998.

[30] A. C. Ugural, *Stresses in plates and shells*. Boston: WCB/McGraw Hill, 1999.

[31] S. A. Prasad *et al.*, "Analytical electroacoustic model of a piezoelectric composite circular plate," *AIAA journal,* vol. 44, no. 10, p. 2311, 2006.

[32] Y. Bai, X. Han, X. C. Zheng, and L. Qiao, "Both high reliability and giant electrocaloric strength in BaTiO(3) ceramics," *Sci Rep,* vol. 3, p. 2895, Oct 8 2013.

[33] Z.-W. Yin, H.-S. Luo, P.-C. Wang, and G.-S. Xu, "Growth, characterization and properties of relaxor ferroelectric PMN-PT single crystals," *Ferroelectrics,* vol. 229, no. 1, pp. 207-216, 1999/05/01 1999.

[34] Y. Bai, D. Wei, and L.-J. Qiao, "Control multiple electrocaloric effect peak in Pb(Mg1/3Nb2/3)O3-PbTiO3 by phase composition and crystal orientation," *Applied Physics Letters,* vol. 107, no. 19, p. 192904, 2015.

[35] R. Wongmaneerung, R. Guo, A. Bhalla, R. Yimnirun, and S. Ananta, "Thermal expansion properties of PMN–PT ceramics," *Journal of Alloys and Compounds,* vol. 461, no. 1, pp. 565-569, 2008/08/11/ 2008.

[36] K. C. Cheng, H. L. W. Chan, C. L. Choy, Q. R. Yin, H. S. Lu, and Z. W. Yin, "Piezoelectric coefficients of PMN-0.33PT single crystals," in *ISAF 2000. Proceedings of the 2000 12th IEEE International Symposium on Applications of Ferroelectrics (IEEE Cat. No.00CH37076)*, 2000, vol. 2, pp. 533-536 vol. 2.

[37] H. Ursic, M. Vrabelj, L. Fulanović, A. Bradeško, S. Drnovšek, and B. Malic, *Specific heat capacity and thermal conductivity of the electrocaloric (1-x)Pb(Mg1/3Nb2/3)O3–xPbTiO3 ceramics between room temperature and 300 °C*. 2016, pp. 260-265.

[38] D. Viehland and J.-F. Li, "Young's modulus and hysteretic losses of 0.7Pb(Mg1/3Nb2/3)O3–0.3PbTiO3: single versus polycrystalline forms," *Journal of Applied Physics,* vol. 94, no. 12, pp. 7719-7722, 2003.

[39] Q.-M. Wang, X. H. Du, B. Xu, and L. Eric Cross, *Electromechanical Coupling and Output Efficiency of Piezoelectric Bending Actuators*. 1999, pp. 638-646.

[40] Z. Liang, C. Xu, B. Ren, and H. Luo, "Theoretical analysis of energy harvesting performance for clamped–clamped piezoelectric beam," *Microsystem Technologies,* journal article vol. 21, no. 4, pp. 815-823, April 01 2015.

[41] M. Sitti, D. Campolo, J. Yan, and R. S. Fearing, "Development of PZT and PZN-PT based unimorph actuators for micromechanical flapping mechanisms," in *Proceedings 2001 ICRA. IEEE International Conference on Robotics and Automation (Cat. No.01CH37164),* 2001, vol. 4, pp. 3839-3846 vol.4.

[42] Z. Sun, Q.-M. Wang, and W. S. Slaughter, "The Solid-State Electrocaloric Refrigeration With Unimorph Beam and its Analytical Model," no. 52118, p. V08AT10A060, 2018.

[43] M. S. Weinberg, "Working equations for piezoelectric actuators and sensors," *Journal of Microelectromechanical Systems,* vol. 8, no. 4, pp. 529-533, 1999.

[44] Y. Hu *et al.*, "Combined caloric effects in a multiferroic Ni–Mn–Ga alloy with broad refrigeration temperature region," *APL Materials,* vol. 5, no. 4, p. 046103, 2017.

[45] S. F. K. A.V. Es'kov, O.V. Pakhomov, A.S. Starkov, "Simulation of a solid-state cooler with electrocaloric elements," *Physics of the Solid State,* vol. 51, no. 8, pp. 1574-1577, 2009.